CHAPTER 44
ATMOSPHERIC OPTICS

Dennis K. Killinger
Center for Laser Atmospheric Sensing
Department of Physics
University of South Florida
Tampa, Florida

James H. Churnside
National Oceanic and Atmospheric Administration
Environmental Technology Laboratory
Boulder, Colorado

Laurence S. Rothman
Air Force Geophysics Directorate/Phillips Lab
Optical Environment Division
Hanscom AFB, Massachusetts

44.1 GLOSSARY

c	speed of light
C_n^2	atmospheric turbulence strength parameter
F	hypergeometric function
$g(v)$	optical absorption lineshape function
h	height above sea level
h	Planck's constant
I	intensity of optical beam (watts/m^2)
J	Bessel function
L_o	outer scale size of atmospheric turbulence
l_o	inner scale size of atmospheric turbulence
N	density or concentration of molecules
P_v	Planck radiation function
R	gas constant
S	molecular absorption line intensity
T	temperature

W	wind speed
β	backscatter coefficient of the atmosphere
γ_p	pressure-broadened half-width of absorption line
κ	optical attenuation
λ	wavelength
ν	optical frequency (wave numbers)
$\rho(I)$	probability density function of irradiance fluctuations
ρ_o	phase coherence length
σ_I^2	variance of irradiance fluctuations
σ_R	Rayleigh scattering cross section

44.2 INTRODUCTION

Atmospheric optics involves the transmission, absorption, emission, refraction, and reflection of light by the atmosphere and is probably one of the most widely observed of all optical phenomena.[1–5] The atmosphere interacts with light due to the composition of the atmosphere, which under normal conditions, consists of a variety of different molecular species and small particles or aerosols. This interaction of the atmosphere with light is observed to produce a wide variety of optical phenomena including the blue color of the sky, the red sunset, the optical absorption of specific wavelengths due to atmospheric molecules, the twinkling of stars at night, and the greenish tint sometimes observed during a severe wind storm due to the high density of dust and water-related aerosols in the atmosphere.

One of the most basic optical phenomena of the atmosphere is the absorption of light. This absorption process can be depicted as in Fig. 1 which shows the transmission spectrum of the atmosphere as a function of wavelength.[5] The transmission of the atmosphere is highly dependent upon the wavelength of the spectral radiation, and, as will be covered later in this chapter, upon the composition and specific optical properties of the
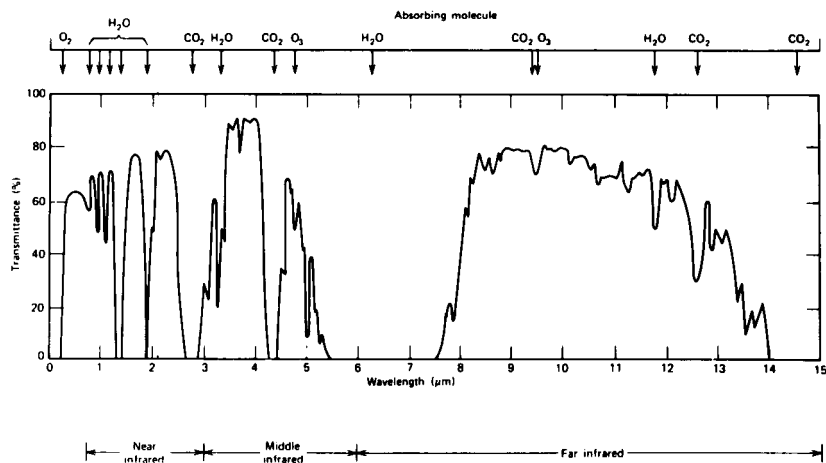

FIGURE 1   Transmittance through the earth's atmosphere as a function of wavelength taken with low spectral resolution (path length 1800 m). (*From Measures, Ref. 5.*)

constituents in the atmosphere. The prominent spectral features in the transmission spectrum in Fig. 1 are primarily due to absorption bands and individual absorption lines of the molecular gases in the atmosphere, while a portion of the slowly varying background transmission is due to aerosol extinction, continuum absorption, and particulates in the atmosphere.

This chapter presents a tutorial overview of some of the basic optical properties of the atmosphere, with an emphasis on those properties associated with optical propagation and transmission of light through the Earth's atmosphere. The physical phenomena of optical absorption, scattering, emission, and refractive properties of the atmosphere will be covered for optical wavelengths from the UV to the far-infrared. The primary focus of this chapter is on *linear* optical properties associated with the transmission of light through the atmosphere. Historically, the study of atmospheric optics has centered around the radiance transfer function of the atmosphere, and the linear transmission spectrum and blackbody emission spectrum of the atmosphere. This emphasis was due to the large body of research associated with passive, electro-optical sensors which primarily use the transmission of ambient optical light or light from selected emission sources. During the past decade, however, the use of lasers has added a new dimension to the study of atmospheric optics. In this case, not only is one interested in the transmission of light through the atmosphere, but also information regarding the optical properties of the backscattered optical radiation.

In this chapter, the standard linear optical interactions of an optical or laser beam with the atmosphere will be covered, with an emphasis placed on linear absorption and scattering interactions. It should be mentioned that the first edition of the OSA *Handbook of Optics* chapter on "Atmospheric Optics" had considerable nomographs and computational charts to aid the user in numerically calculating the transmission of the atmosphere.[2] Because of the present availability of a wide range of spectral databases and computer programs (such as the HITRAN Spectroscopy Database, and LOWTRAN, MODTRAN, and FASCODE atmospheric transmission computer programs) that model and calculate the transmission of light through the atmosphere, these nomographs, while still useful, are not as vital. As a result, the emphasis of this second edition of the "Atmospheric Optics" chapter is on the basic theory of the optical interactions, how this theory is used to model the optics of the atmosphere, the use of available computer programs and databases to calculate the optical properties of the atmosphere, and examples of instruments and meteorological phenomena related to optical or visual remote sensing of the atmosphere.

The overall organization of this chapter begins with a description of the natural, homogeneous atmosphere and the representation of its physical and chemical composition as a function of altitude. A brief survey is then made of the major linear optical interactions that can occur between a propagating optical beam and the naturally occurring constituents in the atmosphere. The next section covers several major computational programs (HITRAN, LOWTRAN, MODTRAN, and FASCODE) and U.S. Standard Atmospheric Models which are used to compute the optical transmission, scattering, and absorption properties of the atmosphere. The next major technical section presents an overview of the influence of atmospheric refractive turbulence on the statistical propagation of an optical beam or wavefront through the atmosphere. Finally, the last two sections of the chapter include a brief introduction to some optical and laser remote sensing experiments of the atmosphere and a brief introduction to the visually important field of meteorological optics.

It should be noted that the material contained within this chapter has been compiled from several recent overview/summary publications on the optical transmission and atmospheric composition of the atmosphere, as well as from a large number of technical reports and journal publications. These major overview references are: (1) the previous edition of the *OSA Handbook of Optics* (chapter on "Optical Properties of the Atmosphere"), (2) *Handbook of Geophysics and the Space Environment* (chapter on "Optical and Infrared Properties of the Atmosphere"), (3) *The Infrared Handbook,* (4) *Laser Remote Sensing,* and (5) *Atmospheric Radiation.*[1–5] The interested reader is directed

toward these comprehensive treatments as well as to the listed references therein for detailed information concerning the topics covered in this brief overview of atmospheric optics.

44.3 PHYSICAL AND CHEMICAL COMPOSITION OF THE STANDARD ATMOSPHERE

The atmosphere is a fluid composed of gases, particulates, and aerosols whose physical and chemical properties vary as a function of time, altitude, and geographical location. Although these properties can be highly dependent upon local and regional conditions, many of the optical properties of the atmosphere can be described to an adequate level by looking at the compositon of what one normally calls a *standard atmosphere.* This section will describe the background, homogeneous standard composition of the atmosphere. This will serve as a basis for the determination of the quantitative interaction of the molecular gases, aerosols, and particulates in the atmosphere with a propagating optical wavefront.

Molecular Gas Concentration, Pressure, and Temperature

The majority of the atmosphere is composed of lightweight molecular gases. Table 1 lists the major gases and trace species of the terrestrial atmosphere, and their approximate concentration in units of atmospheres (atm) at standard room temperature (296 K), altitude at sea level, and total pressure of 1 atm.[6] The major optically active molecular constituents of the atmosphere are N_2, O_2, H_2O, and CO_2, with a secondary grouping of CH_4, N_2O, CO, and O_3. The other 22 species in the table are present in the atmosphere at trace-level concentrations (ppb, down to less than ppt by volume), however the concentration may be increased by many orders of magnitude due to local emission sources of these gases.

The temperature of the atmosphere varies both with seasonal changes and altitude. Figure 2 shows the average temperature profile of the atmosphere as a function of altitude presented for the U.S. Standard atmosphere.[7] The temperature decreases significantly with altitude until the level of the stratosphere is reached where the temperature profile has an inflection point. The U.S. Standard Atmosphere is one of six basic atmospheric models developed by the U.S. government; these different models furnish a good representation of the different atmospheric conditions which are often encountered. Figure 3 shows the temperature profile for the six atmospheric models.[7]

The pressure of the atmosphere decreases with altitude due to the gravitational pull of the earth and the hydrostatic equilibrium pressure of the atmospheric fluid. This is indicated in Fig. 4 which shows the total pressure of the atmosphere in millibars (1013 mb = 1 atm = 760 torr) as a function of altitude for the different atmospheric models.[7] The fractional or partial pressure of most of the major gases (N_2, O_2, CO_2, N_2O, CO, and CH_4) follows this profile and these gases are considered uniformly mixed. However, the concentration of water vapor is very temperature-dependent due to freezing and is not uniformly mixed in the atmosphere. Figure 5a shows the partial pressure (density) of water vapor as a function of altitude; the units of density are in molecules/cm^3 and are related to 1 atm by the appropriate value of Loschmidts number (the number of molecules in 1 cm^3 of air) at a temperature of 296 K, which is 2.479×10^{19} molecules/cm^3.[7]

The partial pressure of ozone (O_3) also varies significantly with altitude because it is generated in the upper altitudes and near ground level by solar radiation, and is in chemical equilibrium with other gases in the atmosphere which themselves vary with altitude and time of day. Figure 5b shows the typical concentration of ozone as a function

TABLE 1 List of Molecular Gases and Their Typical Concentration for the Ambient U.S. Standard Atmosphere (Note that the trace species have concentrations less than 1×10^{-9}, with a value that is variable and often dependent upon local emission sources.)

Molecule	p (atm)
N_2	0.781
O_2	0.209
H_2O	0.0775 (variable)
CO_2	$3.3\,E-4$
A (Argon)	0.0093
CH_4	$1.7\,E-6$
N_2O	$3.2\,E-7$
CO	$1.5\,E-7$
O_3	$2.66\,E-8$ (variable)
H_2CO	$2.4\,E-9$
C_2H_6	$2\,E-9$
HCl	$1\,E-9$
CH_3Cl	$7\,E-10$
OCS	$6\,E-10$
C_2H_2	$3\,E-10$
SO_2	$3\,E-10$
NO	$3\,E-10$
H_2O_2	$2\,E-10$
HCN	$1.7\,E-10$
HNO_3	$5\,E-11$
NH_3	$5\,E-11$
NO_2	$2.3\,E-11$
HOCl	$7.7\,E-12$
HI	$3\,E-12$
HBr	$1.7\,E-12$
OH	$4.4\,E-14$
HF	$1\,E-14$
ClO	$1\,E-14$
HCOOH	$1\,E-14$
COF_2	$1\,E-14$
SF_6	$1\,E-14$
H_2S	$1\,E-14$
PH_3	$1\,E-20$

of altitude.[7] The ozone concentration peaks at an altitude of approximately 20 km and is one of the principal molecular optical absorbers in the atmosphere at that altitude. Further details of these atmospheric models under different atmospheric conditions are contained within the listed references and the reader is encouraged to consult these references for more detailed information.[3,7]

Aerosols and Particulates

The atmospheric propagation of optical radiation is influenced by particulate matter suspended in the air such as dust, fog, haze, cloud droplets, and aerosols. Figure 6 shows
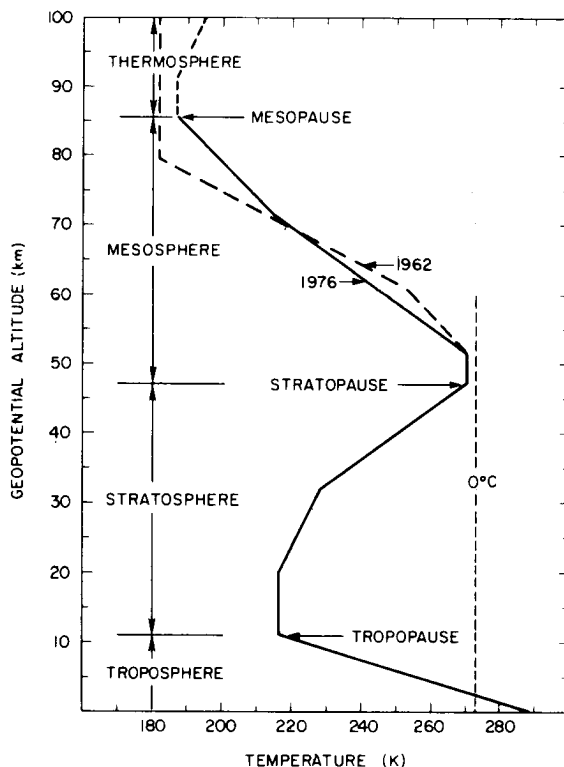
FIGURE 2 Temperature-height profile for U.S. Standard Atmosphere (0–86 km).

the basic characteristics of particulates in the amosphere as a function of altitude,[3] and Fig. 7 indicates the approximate size of common atmospheric particles.[5]

Aerosols in the boundary layer (surface to 1 to 2 km altitude) are locally emitted, wind-driven particulates, and have the greatest variability in composition and concentration. Over land, the aerosols are mostly soil particles, dust, and organic particles from vegetation. Over the oceans, they are mostly sea salt particles. At times, however, long-range global winds are capable of transporting land particulates vast distances across the oceans or continents, especially those particulates associated with dust storms or large biomass fires, so that substantial mixing of the different particulate types may occur.

In the troposphere above the boundary layer, the composition is less dependent upon local surface conditions and a more uniform, global distribution is observed. The aerosols observed in the troposphere are mostly due to the coagulation of gaseous compounds and fine dust. Above the troposphere, in the region of the stratosphere from 10 to 30 km, the background aerosols are mostly sulfate particles and are uniformly mixed globally. However, the concentration can be perturbed by several orders of magnitude due to the injection of dust and SO_2 by volcanic activity, such as the recent eruption of Mount Pinatubo.[8] Such increases in the aerosol concentration may persist for several years and significantly impact the global temperature of the earth.

Several models have been developed for the number density and size distribution of aerosols in the atmosphere.[7] Figures 8 and 9 show two aerosol distribution models appropriate for the rural environment and maritime environment, as a function of relative
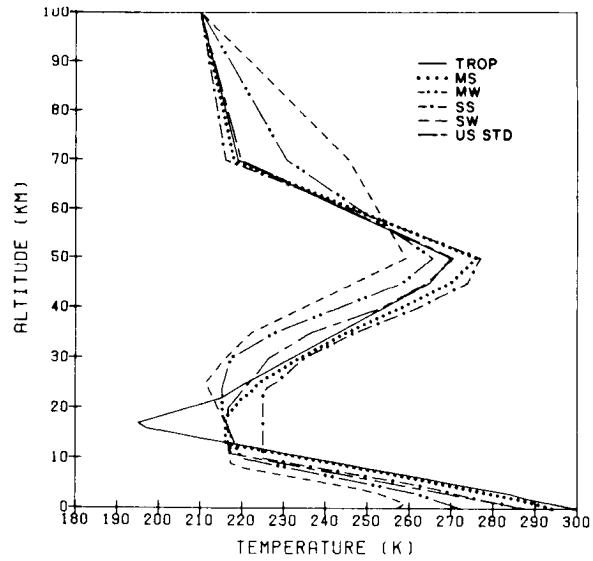
FIGURE 3 Temperature vs. altitude for the six model atmospheres: tropical (TROP), midlatitude summer (MS), midlatitude winter (MW), subarctic summer (SS), subarctic winter (SW), and U.S. standard (US STD).
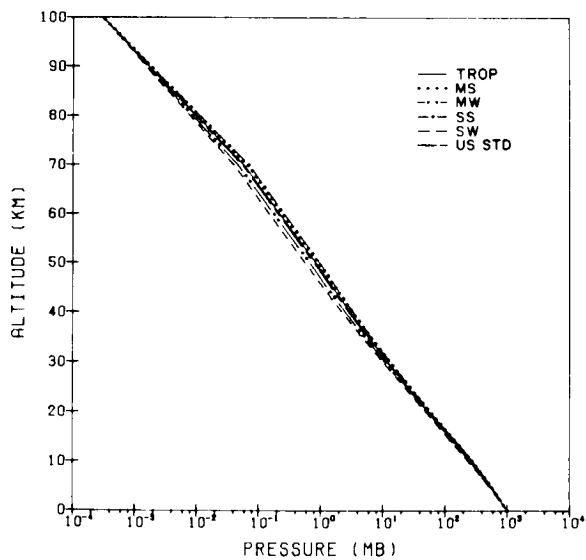

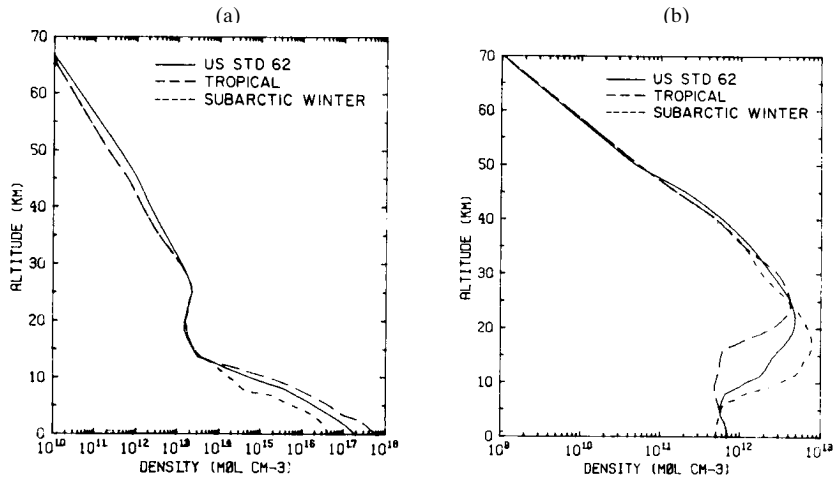**FIGURE 4** Pressure vs. altitude for the six model atmospheres.

FIGURE 5 (*a*) Water vapor profile of several models; (*b*) ozone profile for several models; the U.S. standard model shown is the 1962 model.
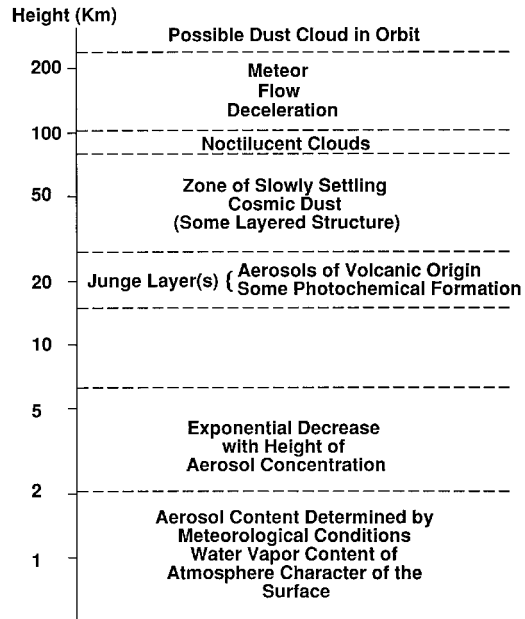

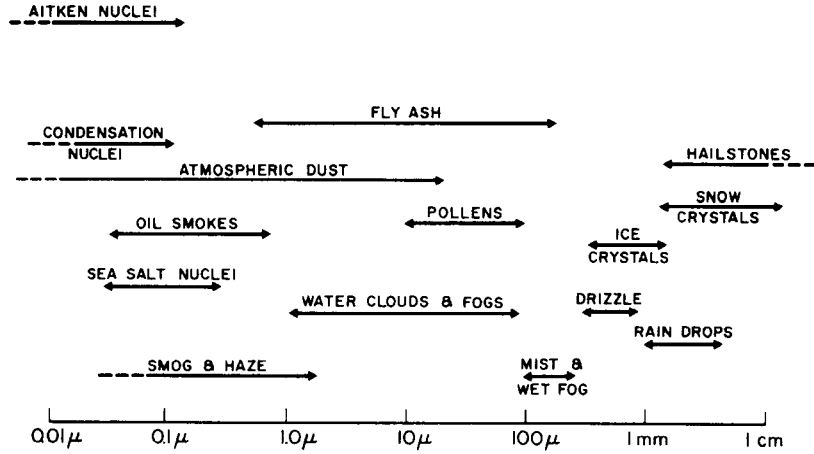**FIGURE 6** Physical characteristics of atmospheric aerosols.

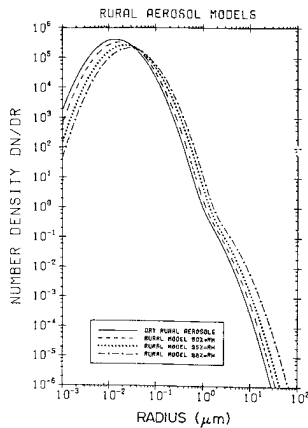**FIGURE 7** Representative diameters of common atmospheric particles. *(From Measures, Ref. 5.)*

FIGURE 8 Aerosol number density distribution $(cm^{-3} \mu m^{-1})$ for the rural model at different relative humidities with total particle concentrations fixed at 15,000 cm^{-3}.

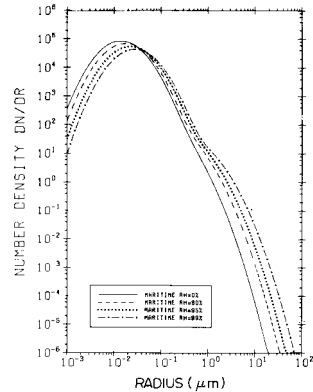**FIGURE 9** Aerosol number density distribution $(cm^{-3} \mu m^{-1})$ for the maritime model at different relative humidities with total particle concentrations fixed at 4000 cm^{-3}.

humidity[7]; the humidity influences the size distribution of the aerosol particles and their growth characteristics. The greatest number density (particles/cm^3) occurs near a size of 0.01 μm but a significant number of aerosols are still present even at the larger sizes near 1 to 2 μm. Finally, the optical characteristics of the aerosols can also be dependent upon water vapor concentration, with changes in surface, size, and growth characteristics of the aerosols sometimes observed to be dependent upon the relative humidity. Such humidity changes can also influence the concentration of some pollutant gases, if these gases have been absorbed onto the surface of the aerosol particles.[7]

44.4   *FUNDAMENTAL THEORY OF INTERACTION OF LIGHT WITH THE ATMOSPHERE*

The propagation of light through the atmosphere depends upon several optical interaction phenomena and the physical composition of the atmosphere. In this section, we consider some of the basic interactions involved in the transmission, absorption, emission, and scattering of light as it passes through the atmosphere. Although all of these interactions can be described as part of an overall radiative transfer process, it is common to separate the interactions into distinct optical phenomena of molecular absorption, Rayleigh scattering, Mie or aerosol scattering, and molecular emission. Each of these basic phenomena will be discussed in this section following a brief outline of the fundamental equations for the transmission of light in the atmosphere centered around the Beer-Lambert law.

The linear transmission (or absorption) of monochromatic light by species in the atmosphere may be expressed approximately by the Beer-Lambert law as

$$I(\lambda, t', x) = I(\lambda, t, 0)e^{-\int_0^x \kappa(\lambda)N(x', t)\, dx'} \tag{1}$$

where $I(\lambda, t', x)$ is the intensity of the optical beam after passing through a path length of x, $\kappa(\lambda)$ is the optical attenuation or extinction coefficient of the species per unit of species density and length, and $N(x, t)$ is the spatial and temporal distribution of the species density that is producing the absorption; λ is the wavelength of the monochromatic light, and the parameter time t' is inserted to remind one of the potential propagation delay. Equation (1) contains the term $N(x, t)$ which explicitly indicates the spatial and temporal variability of the concentration of the attenuating species since in many experimental cases such variability may be a dominant feature.

It is common to write the attenuation coefficient in terms of coefficients that can describe the different phenomena that can cause the extinction of the optical beam. The most dominant interactions in the natural atmosphere are those due to Rayleigh (elastic) scattering, linear absorption, and Mie (aerosol/particulate) scattering; elastic means that the scattered light does not change in wavelength from that which was transmitted while inelastic infers a shift in the wavelength. In this case, one can write $\kappa(\lambda)$ as

$$\kappa(\lambda) = \kappa_a(\lambda) + \kappa_R(\lambda) + \kappa_M(\lambda) \tag{2}$$

where these terms represent the individual contributions due to absorption, Rayleigh scattering, and Mie scattering, respectively. The values for each of these extinction coefficients will be described in the following sections along with the appropriate species

density term $N(x, t)$. In some of these cases, the reemission of the optical radiation, possibly at a different wavelength, is also of importance. Rayleigh extinction will lead to Rayleigh backscatter, Raman extinction leads to spontaneous Raman scattering, absorption can lead to fluorescence emission or thermal heating of the molecule, and Mie extinction is defined primarily in terms of the scattering coefficient. Under idealized conditions, the scattering processes can be related directly to the value of the attenuation processes. However, if several complex optical processes occur simultaneously, such as in atmospheric propagation, the attenuation and scattering processes are not directly linked via a simple analytical equation. In this case, independent measurements of the scattering coefficient and the extinction coefficient have to be made, or approximation formulas are used to relate the two coefficients.[4,5]

Molecular Absorption

The absorption of optical radiation by molecules in the atmosphere is primarily associated with individual optical absorption transitions between the allowed quantized energy levels of the molecule. The energy levels of a molecule can usually be separated into those associated with rotational, vibrational, or electronic energy states. Absorption transitions between the rotational levels occur in the far-IR and microwave spectral region, transitions between vibrational levels occur in the near-IR (2 to 20 μm wavelength), and electronic transitions occur in the UV-visible region (0.3 to 0.7 μm). Transitions can occur which combine several of these categories, such as rotational-vibrational transitions or electronic-vibrational-rotational transitions.

Some of the most distinctive and identifiable absorption lines of many atmospheric molecules are the rotational-vibrational optical absorption lines in the infrared spectral region. These lines are often clustered together into vibrational bands according to the allowed quantum transitions of the molecule. In many cases, the individual lines are distinct and can be resolved if the spectral resolution of the measuring instrument is fine enough (i.e., $<0.1 \text{ cm}^{-1}$). An example of such a region is the absorption feature near 2.04 μm in Fig. 1 which is actually composed of individual absorption lines if viewed under higher spectral resolution. Figure 10 is a computed high-resolution expansion of the
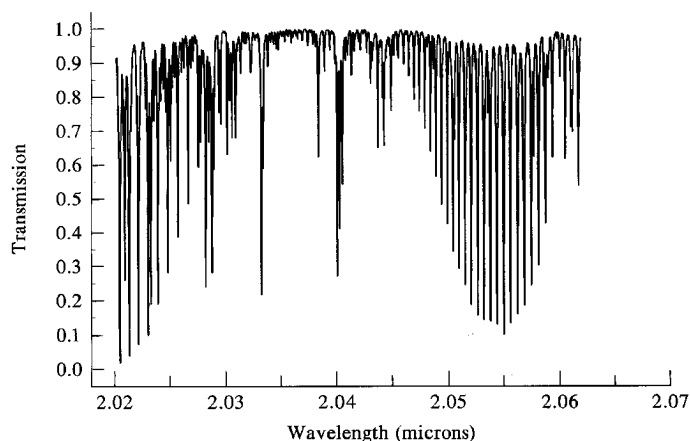

FIGURE 10   High-resolution transmission spectrum of the atmosphere for a horizontal path of 1800 m (similar to that in Fig. 1) for the spectral region near 2.04 μm. The individual rotational absorption lines due to CO_2 and H_2O are easily observed.
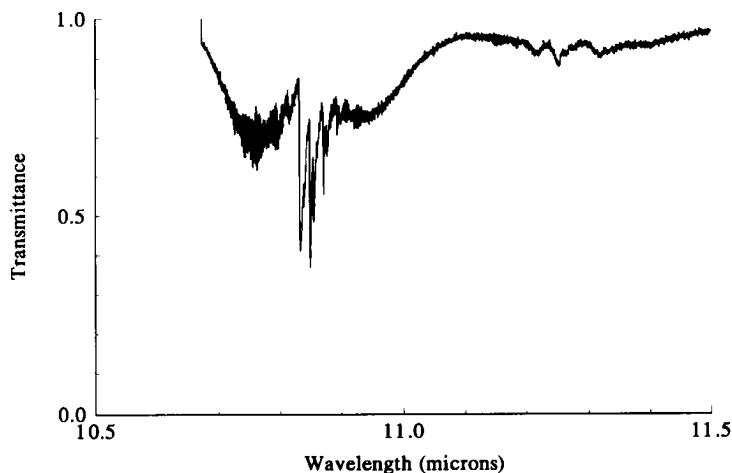
FIGURE 11 High-resolution absorption spectrum of Freon-12 gas showing complex band structure typical of heavy, complex molecules in the atmosphere (path of 1000 m with 1 ppm concentration).

atmospheric spectrum of Fig. 1 near 2.04 μm over a path length of 1800 m which shows these individual lines. In this case, the individual lines are well-separated and appear like a "picket fence" spectrum showing gaps between the absorption lines. Many of the atmospheric gaseous molecules listed earlier in Table 1 have similar spectral structure. These gases are relatively lightweight and have few (less than 5 or 6) atoms per molecule so that their moments of inertia are relatively small. The resulting energy spacing between the allowed rotational-vibrational absorption transitions is large and well-separated in wavelength.

In other spectral regions, however, the individual lines overlap or are so strong or saturated that the transmission spectrum displays only broad spectral features; an example of such a spectral region is the strong absorption seen near 2.7 μm, 5 to 8 μm, and beyond 13 μm in Fig. 1. Finally, the molecular absorption observed in the UV is often due to optical transitions to an electronic energy level, molecular energy continuum or a predissociation energy level. In some cases, such as that for O_3 or SO_2, this results in broad absorption bands that extend throughout the UV region (250 to 350 nm).

More complex, heavier molecules, such as benzene or chlorofluorocarbons, have absorption spectra which are blended or merged together into band spectra due to the complexity and overlap of the rotational-vibrational transitions of these molecules. Figure 11 shows a transmission spectrum of Freon-12 ($C Cl_2 F_2$) which has a complex spectrum near 11 μm. As seen, the individual rotational lines are merged into a band spectrum. A band spectrum is often unique for each gas and can be used to identify the chemical composition of the gas. Heavy molecules in the atmosphere are not normally part of the natural atmosphere and are usually the result of pollution or gaseous plumes injected into the atmosphere.

The overall transmission or absorption of the atmosphere due to an individual molecular absorption line can be given quantitatively as

$$\kappa_a(\lambda)N(x, t) = Sg(v - v_o)NP_a \tag{3}$$

where S is the molecular transition line intensity (units of cm/molecule), $g(v - v_o)$ is the normalized lineshape function (units of cm or $1/cm^{-1}$), N is the number of molecules of absorbing species per cm^3 per atm, and P_a is the partial pressure of the absorbing gas in

atm. The value of N is equal to the value of Loschmidt's number, which is 2.479 $\times 10^{19}$ molecules cm^{-3} atm^{-1} at a temperature of 296 K; The value of N is inversely proportional to temperature due to the change in gas concentration as a function of temperature for 1 atm of pressure. As will be seen later, the definition of S as given in Eq. (3) is that used in the U.S. Air Force Phillips Laboratory/Geophysics Directorate HITRAN database.[9] In this case, S contains the Boltzmann population factor and isotope fraction (natural abundance) as well as the stimulated emission term due to finite population in the upper energy states of the molecule.[9] In Eq. (3), $Sg(v - v_o)$ is the absorption cross section per molecule (cm^2/molecule) and NP_a is the number of absorbing molecules in units of molecules/cm^3.

The lineshape function can be described by several different models. The two most prevalent are the lorentzian lineshape associated with pressure broadening and the gaussian lineshape associated with Doppler broadening which becomes important at elevated temperatures or low pressures.

The lorentzian/pressure-broadened profile is given by

$$g_L(v - v_o) = (\gamma_p/\pi)/[(v - v_o)^2 + \gamma_P^2] \tag{4}$$

where γ_p is the pressure-broadened half-width at half-maximum (HWHM) in wave numbers (cm^{-1}). The pressure-broadened half-width is obtained from the air-broadened half-width parameter g as $\gamma_p = gP_t$, where P_t is the total background atmospheric pressure. Under ambient atmospheric conditions, g is approximately 0.05 cm^{-1} (i.e., 1.5 GHz) for many molecules in the atmosphere.

It should be noted that under very low pressure conditions, where the time between collisions with other molecules is relatively long, the intrinsic radiative lifetime of the molecule will determine the lineshape profile. Under these conditions, the linewidth is called the natural linewidth. The natural linewidth of many molecules is on the order of a few MHz (i.e., approximately 0.0001 cm^{-1}) or less.

The gaussian or Doppler line profile is expressed as

$$g_D(v - v_o) = (1/\gamma_D)(\ln 2/\pi) . 5 \exp\left[-\ln 2(v - v_o)^2/\gamma_D^2\right] \tag{5}$$

where γ_D is the Doppler linewidth (HWHM in cm^{-1}) given by

$$\gamma_D = (v_o/c)[2RT \ln 2/M]^{1/2} \tag{6}$$

where R is the gas constant, T is the temperature in Kelvin, and M is the molecular weight of the molecule.

The value for the lineshape at the peak (line center) is equal to $1/(\pi\gamma_p) = 0.318/\gamma_p$ for the pressure-broadened case. For the Doppler peak, the maximum value is $(\ln 2/\pi)^{1/2}/\gamma_D = 0.469/\gamma_D$. Under ambient atmospheric conditions, the Doppler linewidth is usually much smaller than the pressure-broadened linewidth.

For those cases where both lorentzian and Doppler broadening are present in approximately equal amounts, a convolution of the Doppler and lorentzian profile must be used. This convolution of a Doppler and lorentzian is called a Voigt profile and involves a double integral for an exact calculation. Fortunately, several numerical approximations are available for the computation of the Voigt profile and lineshape parameters.[10] The Voigt profile is important in the spectroscopy of molecules in the upper atmosphere where the ambient pressure is low and the Doppler and pressure-broadened linewidths are of the same order of magnitude.

Finally, the large number of transition lines of water vapor and other gases in the atmosphere can produce a significant level of background "quasi-continuum" absorption in the atmosphere. This phenomenon is primarily due to the additive contribution from the wings of the absorption lines even at wavelengths far removed (100 s of cm^{-1}) from the line centers. Such an effect has been studied by Burch and by Clough et al. for water
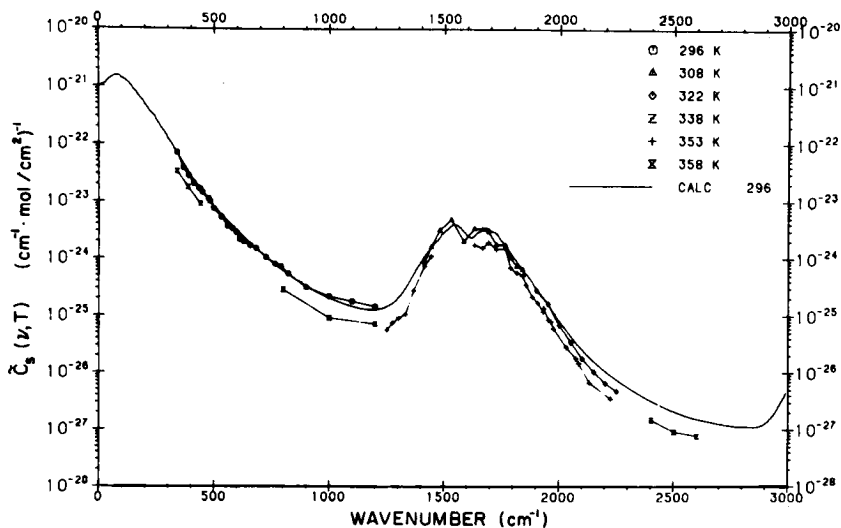
FIGURE 12   Self-density absorption continuum values C_s for water vapor as a function of wave number. The experimental values were measured by Burch. *(From Ref. 3.)*

vapor due to strong self-broadening interactions.[11] Figure 12 shows a plot of the relative continuum coefficient for water vapor as a function of wave number. Good agreement with the experimental data and model calculations is shown. Models for water vapor and nitrogen continuum absorption are contained within many of the major atmospheric transmission programs (such as FASCODE). The typical value for the continuum absorption is negligible in the visible to the near-IR, but can be significant at wavelengths in the range of 5 to 20 μm.

Molecular Rayleigh Scattering

Rayleigh scattering is elastic scattering of the optical radiation due to the displacement of the weakly bound electronic cloud surrounding the gaseous molecule which is perturbed by the incoming electro-magnetic (optical) field. This phenomenon is associated with optical scattering where the wavelength of light is much larger than the physical size of the scatterers (i.e., atmospheric molecules). Rayleigh scattering, which makes the color of the sky blue and the setting or rising sun red, was first described by Lord Rayleigh in 1871. The Rayleigh differential scattering cross section for polarized, monochromatic light is given by[5]

$$d\sigma_R/d\Omega = [\pi^2(n^2-1)^2/N^2\lambda^4][\cos^2\phi\cos^2\theta + \sin^2\phi] \tag{7}$$

where n is the index of refraction of the atmosphere, N is the density of molecules, λ is the wavelength of the optical radiation, and ϕ and θ are the spherical coordinate angles of the scattered polarized light referenced to the direction of the incident light. As seen from Eq. (7), shorter-wavelength light (i.e., blue) is more strongly scattered out from a propagating beam than the longer wavelengths (i.e., red), which is consistent with the preceding comments regarding the color of the sky or the sunset. A typical value for $d\sigma_R/d\Omega$ at a wavelength of 700 nm in the atmosphere (STP) is approximately 2×10^{-28} cm^2 sr^{-1}.[3] This value depends upon the molecule and has been tabulated for many of the major gases in the atmosphere.[10–12]

The total Rayleigh scattering cross section can be determined from Eq. (7) by integrating over 4π steradians to yield

$$\sigma_R \text{ (total)} = [8/3][\pi^2(n^2-1)^2/N^2\lambda^4] \tag{8}$$

At sea level (and room temperature, $T = 296$ K) where $N = 2.5 \times 10^{19}$ molecules/cm³, Eq. (8) can be multiplied by N to yield the total Rayleigh scattering extinction coefficient as

$$\kappa_R(\lambda)N(x, t) = N\sigma_R(\text{total}) = 1.18 \times 10^{-8} [550 \text{ nm}/\lambda(\text{nm})]^4 \text{ cm}^{-1} \tag{9}$$

The neglect of the effect of dispersion of the atmosphere (variation of the index of refraction n with wavelength) results in an error of less than 3 percent in Eq. (9) in the visible wavelength range.[5]

The molecular Rayleigh backscatter ($\theta = \pi$) cross section for the atmosphere has been given by Collins and Russell for polarized incident light (and received scattered light of the same polarization) as[12]

$$\sigma_R = 5.45 \times 10^{-28} [550 \text{ nm}/\lambda(\text{nm})]^4 \text{ cm}^2 \text{ sr}^{-1} \tag{10}$$

At sea level where $N = 2.47 \times 10^{19}$ molecules/cm³, the atmospheric volume backscatter coefficient, β_R, is thus given by

$$\beta_R = N\sigma_R = 1.39 \times 10^{-8} [550 \text{ nm}/\lambda(\text{nm})]^4 \text{ cm}^{-1} \text{ sr}^{-1} \tag{11}$$

The backscatter coefficient for the reflectivity of a laser beam due to Rayleigh backscatter is determined by multiplying β_R by the range resolution or length of the optical interaction being considered.

For unpolarized incident light, the Rayleigh scattered light has a depolarization factor δ which is the ratio of the two orthogonal polarized backscatter intensities. δ is usually defined as the ratio of the perpendicular and parallel polarization components measured relative to the direction of the incident polarization. Values of δ depend upon the anisotropy of the molecules or scatters, and typical values range from 0.02 to 0.11.[13] Depolarization also occurs for multiple scattering and is of considerable interest in laser or optical transmission through dense aerosol clouds.[14] The depolarization factor can sometimes be used to determine the physical and chemical composition of the cloud constituents, such as the relative ratio of water vapor or ice crystals in a cloud.

Mie Scattering: Aerosols, Particulates, and Clouds

Mie scattering is similar to Rayleigh scattering, except the size of the scattering sites is on the same order of magnitude as the wavelength of the incident light, and is, thus, due to aerosols and fine particulates in the atmosphere. The scattered radiation is the same wavelength as the incident light but experiences a more complex functional dependence upon the interplay of the optical wavelength and particle size distribution than that seen for Rayleigh scattering.

In 1908, Mie investigated the scattering of light by dielectric spheres of size comparable to the wavelength of the incident light.[15] His analysis indicated the clear asymmetry between the forward and backward directions, where for large particle sizes the forward-directed scattering dominates. Complete treatments of Mie scattering can be found in several excellent works by Deirmendjian and others, which take into account the complex index of refraction and size distribution of the particles.[16,17] These calculations are also influenced by the asymmetry of the aerosols or particulates which may not be spherical in shape.

The effect of Mie scattering in the atmosphere can be described as in the following figures. Figure 13 shows the aerosol Mie extinction coefficient as a function of wavelength for several atmospheric models, along with a typical Rayleigh scattering curve for
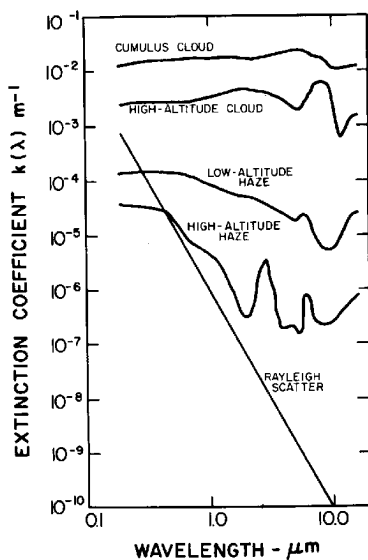
FIGURE 13 Aerosol extinction coefficient as a function of wavelength. *(From Measures, Ref. 5.)*
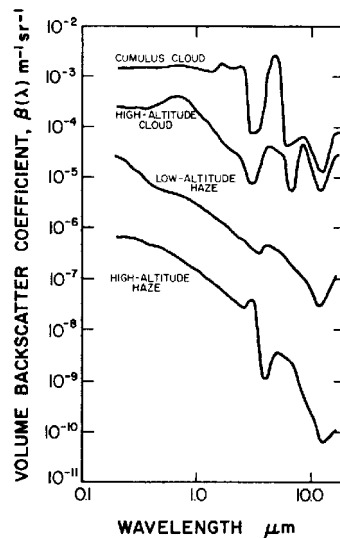
FIGURE 14 Aerosol volume backscattering coefficient as a function of wavelength. *(From Ref. 5.)*

comparison.[18] Figure 14 shows similar values for the volume Mie backscatter coefficient as a function of wavelength.[18] Extinction and backscatter coefficient values are highly dependent upon the wavelength and particulate composition.

Figures 15 and 16 show the calculated extinction coefficient for the rural and maritime aerosol models described in Sec. 44.3 as a function of relative humidity and wavelength.[3] Significant changes in the backscatter can be produced by relatively small changes in the humidity.

The extinction coefficient is also a function of altitude, following the dependence of the composition of the aerosol and particulates. Figure 17 shows an atmospheric aerosol extinction model as a function of altitude for a wavelength of 0.55 μm.[3,8] The influence of the visibility (in km) at ground level dominates the extinction value at the lower altitudes and the composition and density of volcanic particulate dominates the upper altitude regions. The dependence of the extinction on the volcanic composition at the upper altitudes is shown in Fig. 18 which shows these values as a function of wavelength and of composition.[3,8]

The variation of the backscatter coefficient as a function of altitude is shown in Fig. 19 which displays atmospheric backscatter data obtained by McCormick using a 1.06-μm Nd:YAG Lidar.[19] The boundary layer aerosols dominate at the lower levels and the decrease in the atmospheric particulate density determines the overall slope with altitude. Of interest is the increased value near 20 km due to the presence of volcanic aerosols in the atmosphere due to the eruption of Mt. Pinatubo in 1991.

Molecular Emission and Thermal Spectral Radiance

The same optical molecular transitions that cause absorption also emit light when they are thermally excited. Since the molecules have a finite temperature T they will act as blackbody radiators with optical emission given by the Planck radiation law. The allowed transitions of the molecules will modify the intensity distribution of the radiation due to emission of the radiation according to the thermal distribution of the population within
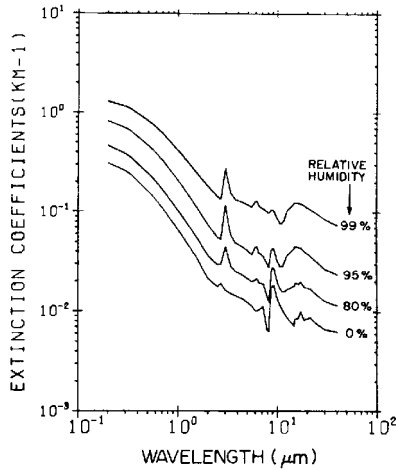
FIGURE 15 Extinction coefficients vs. wavelength for the rural aerosol model for different relative humidities and constant number density of particles.
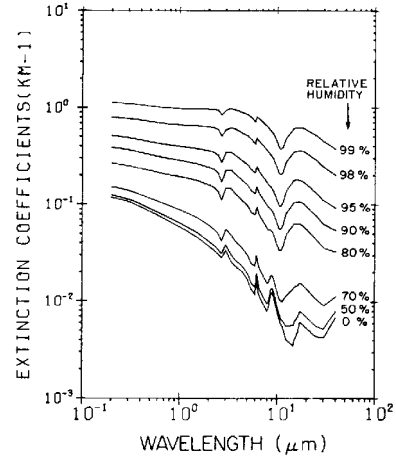
FIGURE 16 Extinction coefficients vs. wavelength for the maritime aerosol model for different relative humidities and constant number density of particles.

the energy levels of the molecule; it should be noted that the Boltzmann thermal population distribution is essentially the same as that which is described by the Planck radiation law for local thermodynamic equilibrium conditions. As such, the molecular emission spectrum of the radiation is similar to that for absorption. The thermal radiance from the clear atmosphere involves the calculation of the blackbody radiation emitted by each elemental volume of air multiplied by the absorption spectral distribution of the molecular absorption lines, $\kappa_a(s)$, and then this emission spectrum is attenuated by the rest of the atmosphere as the emission propagates toward the viewer. This may be expressed as

$$I_\nu = \int_0^s \kappa_a(s) P_\nu(s) \exp\left[-\int_0^s \kappa_a(s')\,ds'\right] ds \qquad (12)$$

where the exponential term is Beer's law, and $P_\nu(s)$ is the Planck function given by

$$P_\nu(s) = 2h\nu^3/[c^2 \exp([h\nu/kT(s)] - 1)] \qquad (13)$$

In these equations, s is the distance from the receiver along the optical propagation path, ν is the optical frequency, h is Planck's constant, c is the speed of light, k is Boltzmann's constant, and $T(s)$ is the temperature at position s along the path. As seen in Eq. (12), each volume element emits thermal radiation of $\kappa_a(s)P_\nu(s)$, which is then attenuated by Beer's law. The total emission spectral density is obtained by summing or integrating over all the emission volume elements and calculating the appropriate absorption along the optical path for each element.

As an example, Fig. 20 shows a plot of the spectral radiance measured on a clear day with $1\,\text{cm}^{-1}$ spectral resolution. Note that the regions of strong absorption produce more radiance as the foregoing equation suggests, and that regions of little absorption correspond to little radiance. In the 800 to 1200 wave number spectral region (i.e., 8.3- to 12.5-μm wavelength region), the radiance is relatively low. This is consistent with the fact that the spectral region from 8 to 12 μm is a transmission window of the atmosphere with relatively little absorption of radiation.
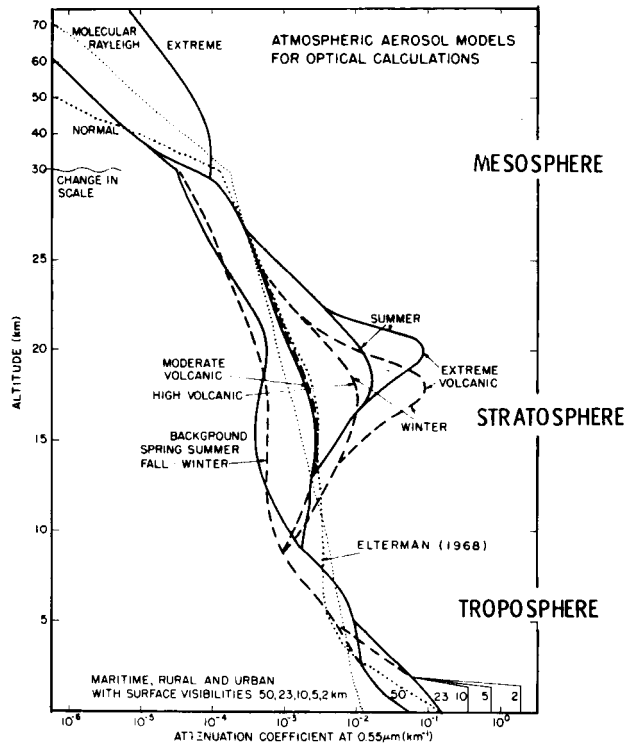
FIGURE 17 The vertical distribution of the aerosol extinction coefficient (at 0.55-μm wavelength) for the different atmospheric models. Also shown for comparison are the Rayleigh profile (dotted line). Between 2 and 30 km, where the distinction on a seasonal basis is made, the spring-summer conditions are indicated with a solid line and fall-winter conditions are indicated by a dashed line. *(From Ref. 3.)*

Surface Reflectivity and Multiple Scattering

The spectral intensity of naturally occurring light at the earth's surface is primarily due to the incident intensity from the sun in the visible to mid-IR wavelength range, and due to thermal emission from the atmosphere and background radiance in the mid-IR. In both cases, the optical radiation is affected by the reflectance characteristics of the clouds and surface layers. For instance, the fraction of light that falls on the earth's surface and is reflected back into the atmosphere is dependent upon the reflectivity of the surface, the incident solar radiation (polarization and spectral density), and the absorption of the atmosphere.

The reflectivity of a surface, such as the earth's surface, is often characterized using the bidirectional reflectance function (BDRF). This function accounts for the nonspecular reflection of light from common rough surfaces and describes the changes in the reflectivity of a surface as a function of the angle which the incident beam makes with the surface. In addition, the reflectivity of a surface is usually a function of wavelength. This latter effect can be seen in Fig. 21 which shows the reflectance of several common substances for normal incident radiation.[2] As seen in Fig. 21, the reflectivity of these surfaces is a strong function of wavelength.
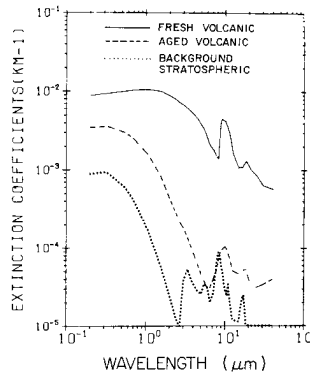
FIGURE 18 Extinction coefficients for the different stratospheric aerosol models (background, volcanic, and fresh volcanic). The extinction coefficients have been normalized to values around peak levels for these models.
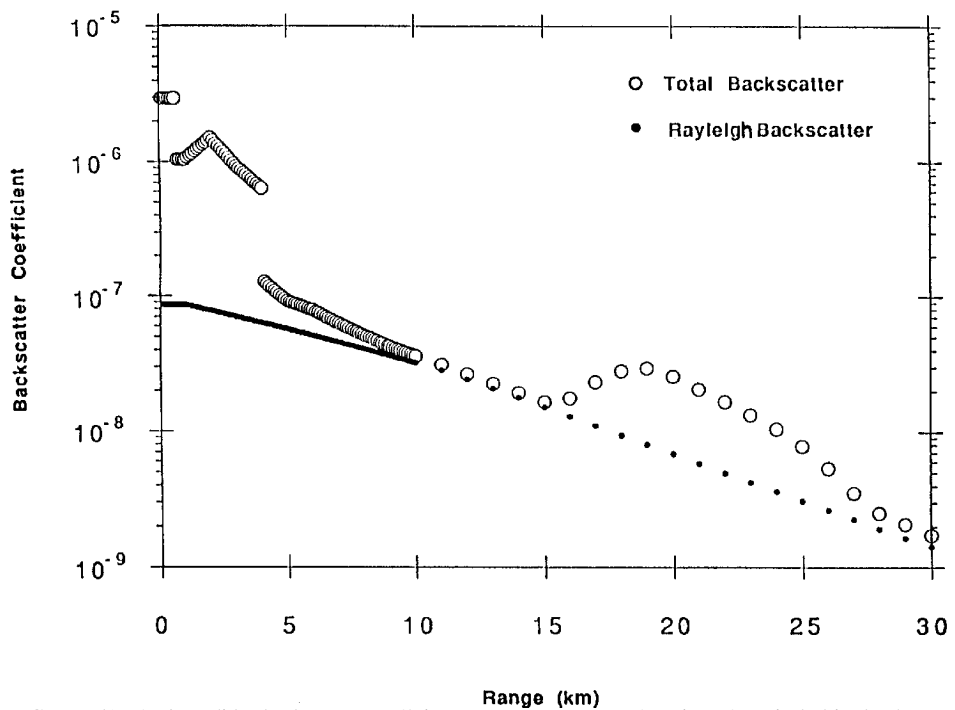

FIGURE 19 1.06-μm lidar backscatter coefficient measurements as a function of vertical altitude. *(From McCormick and Winker, Ref. 19.)*
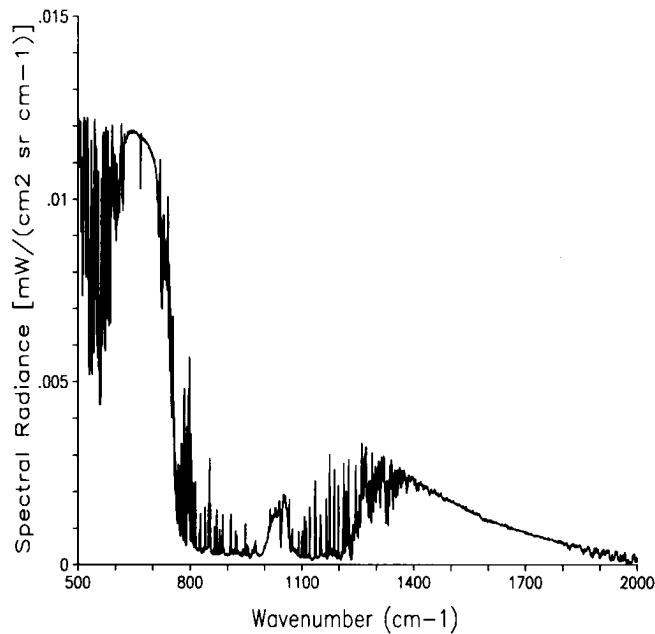
FIGURE 20   Spectral radiance (molecular thermal emission) measured on a clear day showing the relatively low value of radiance near $1000 \, \text{cm}^{-1}$ (i.e., 10-μm wavelength). *(Provided by Churnside.)*
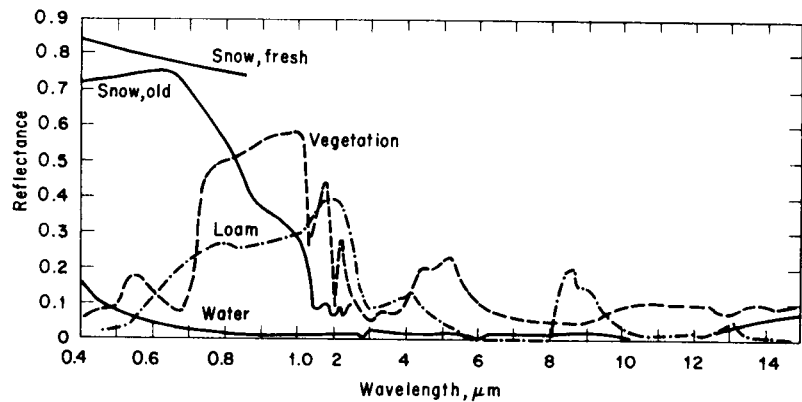

FIGURE 21   Typical reflectance of water surface, snow, dry soil, and vegetation. *(From Ref. 2.)*

The effect of multiple scattering sometimes must be considered when the scattered light undergoes more than one scatter event, and is rescattered on other particles or molecules. These multiple scattering events increase with increasing optical thickness and produce deviations from the Beer-Lambert law. Extensive analyses of the scattering processes for multiple scattering have been conducted and have shown some success in predicting the overall penetration of light through a thick dense cloud. Different computational techniques have been used including the Gauss-Seidel Iterative Method, Layer Adding Method, and Monte-Carlo Techniques.[3,5]

Additional Optical Interactions

In some optical experiments on the atmosphere, a laser beam is used to excite the molecules in the atmosphere to emit inelastic radiation. Two important inelastic optical processes for atmospheric remote sensing are fluorescence and Raman scattering.[5,20]

For the case of laser-induced fluorescence, the molecules are excited to an upper energy state and the reemitted photons are detected. In these experiments, the inelastic fluorescence emission is red-shifted in wavelength and can be distinguished in wavelength from the elastic scattered Rayleigh or Mie backscatter. Laser-induced fluorescence is mostly used in the UV to visible spectral region; collisional quenching is quite high in the infrared so that the fluorescence efficiency is higher in the UV-visible than in the IR. Laser-induced fluorescence is sometimes reduced by saturation effects due to stimulated emission from the upper energy levels. However, in those cases where laser-induced fluorescence can be successfully used, it is one of the most sensitive optical techniques for the detection of atomic or molecular species in the atmosphere.

Laser-induced Raman scattering of the atmosphere is a useful probe of the composition and temperature of concentrated species in the atmosphere. The Raman-shifted emitted light is often weak due to the relatively small cross section for Raman scattering. However, for those cases where the distance is short from the laser to the measurement cloud, or where the concentration of the species is high, it offers significant information concerning the composition of the gaseous atmosphere.

The use of an intense laser beam can also bring about nonlinear optical interactions as the laser beam propagates through the atmosphere. The most important of these are stimulated Raman scattering, thermal blooming, dielectric breakdown, and harmonic conversion. Each of these processes requires a tightly focused laser beam to initiate the nonlinear optical process. The reader is referred to Refs. 21 and 22 for information on these nonlinear optical processes.

44.5 PREDICTION OF ATMOSPHERIC OPTICAL TRANSMISSION: COMPUTER PROGRAMS AND DATABASES

During the past decade, several computer programs and databases have been developed which are very useful for the determination of the optical properties of the atmosphere. Many of these are based upon an ongoing program at the U.S. Air Force Geophysics Laboratory (AFGL), Phillips Laboratory, which has compiled extensive databases for the modeling of atmospheric optical phenomena. The latest versions of these programs and databases are the HITRAN database, FASCODE computer program, and the LOWTRAN or MODTRAN computer code. In addition, several PC (personal computer) versions of these database/computer programs have recently become available so that the user can easily use these computational aids.

The HITRAN database contains the spectroscopic optical parameters of over 30 different molecules in the atmosphere and lists these parameters for over 709,000 separate

absorption lines from a wavelength of 0.44 μm to the microwave region.[9] The data contained in the database include the transition frequencies (or wave number v), line intensity S, linewidth, transition probabilities, and energy levels of the transitions, along with 10 other parameters for each transition line. The HITRAN database has recently been updated in 1992, and a new version is expected in 1994 or 1995.

The FASCODE program calculates the high-resolution transmission spectrum of the atmosphere using the HITRAN database as input.[23,24] It uses computational algorithms to speed the computations of the line-by-line spectra, and contains information for calculating the continuum molecular extinction. FASCODE also calculates the radiance and transmittance of atmospheric slant paths, and can calculate the integrated transmittance through the atmosphere from the ground up to higher altitudes. Voigt lineshape profiles are also used to handle the transition from pressure-broadened lineshapes near ground level to the Doppler-dominated lineshapes at very high altitudes. Several representative models of the atmosphere are contained within FASCODE, so that the user can specify different seasonal and geographical models.

The LOWTRAN computer program calculates the low-resolution (broadband) transmission spectrum and background radiance of the atmosphere at moderate resolution $(20 \text{ cm})^{-1}$.[25,26] Molecular absorption, Rayleigh scattering, and aerosol extinction are computed. Slant path geometry can be specified. LOWTRAN contains many representative atmospheric models (geographical and seasonal), so that the user can see the differences between rural, maritime, winter, tropical, etc. models. Finally, it should be noted that a higher-resolution version of LOWTRAN, called MODTRAN, has recently been released, which calculates the transmission of the atmosphere with a resolution from 2 to 20 cm^{-1}.

Molecular Absorption Line Database: HITRAN

The HITRAN database contains optical spectral data on most of the major molecules in the atmosphere; details of HITRAN are covered in several recent journal articles.[9] The molecules contained in HITRAN are those given previously in Table 1, and cover the spectral range from 0.000001 cm^{-1} to $22,656 \text{ cm}^{-1}$ (i.e., 0.4414 μm to 10^{10} μm). A copy of this database on magnetic tape can be obtained from the U.S. government, and has recently (1992) been put onto CD-ROM optical disks.[27] Each line in the database contains 14 molecular data items that consist of the molecule formula code, isotope type, transition frequency (cm^{-1}), line intensity S in cm/molecule, transition probability, air-broadened half-width (cm^{-1}/atm), self-broadened half-width (cm^{-1}/atm), lower state energy (cm^{-1}), temperature coefficient for air-broadened linewidth, upper-state global quanta index, lower-state global quanta index, upper- and lower-state quanta, error codes, and reference numbers. The density of the lines of the HITRAN database is shown in Fig. 22.

Figure 23 shows an output from a computer program that was used to search the HITRAN database and display some of the pertinent information. The data in HITRAN are in sequential order by transition frequency in wave numbers, and list the molecular name, isotope, absorption line strength S, transition probability R, air-pressure-broadened linewidth γ_g, lower energy state E'', and upper/lower quanta for the different molecules and isotopic species in the atmosphere.

Line-by-line Transmission Program: FASCODE

FASCODE is a large, sophisticated computer program that uses molecular absorption equations (similar to those under ''Molecular Absorption'') and the HITRAN database to calculate the high-resolution spectra of the atmosphere. The FASCODE program includes the effects of the continuum, Rayleigh and aerosol scattering, spectral radiance, slant
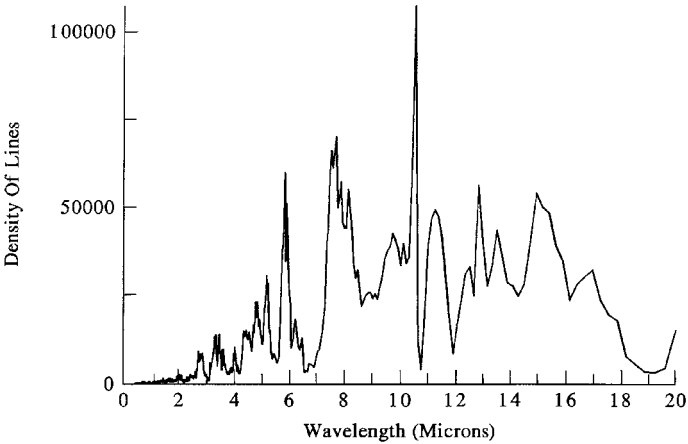
FIGURE 22 Density of absorption lines in HITRAN spectral database.

paths, and altitude density profiles. FASCODE generates the transmission, emission, and radiance of the atmosphere at a spectral resolution which is essentially infinite (i.e., $<0.0001\ \text{cm}^{-1}$).[24] Figure 24 shows a sample output generated from data produced from the FASCODE program and a comparison with experimental data obtained by J. Dowling at NRL.[23] As can be seen, the agreement is very good.

Broadband Transmission: LOWTRAN and MODTRAN

The LOWTRAN computer program does not use the HITRAN database directly, but uses absorption band models to calculate the moderate resolution ($20\ \text{cm}^{-1}$) transmission spectrum of the atmosphere. LOWTRAN uses extensive band-model calculations to speed up the computations, and provides an accurate and rapid means of estimating the transmittance and background radiance of the earth's atmosphere over the spectral

M	I	wn(cm-1)	S	R	g	E''	Q'	Q''
CO2	1	5000.05657	3.963E-27	6.206E	-6.0720	2783.34814		P 33
CO2	3	5000.06953	1.814E-26	1.495E	-6.0703	975.59039		P 51
CO2	1	5000.22347	1.477E-25	8.707E	-6.0674	2240.23755		R 63
H2O	1	5000.22500	2.160E-24	1.860E	-4.0008	2358.30396	14 014	15 015
CO2	2	5000.33473	1.649E-26	1.086E	-5.0894	1390.12122		R 8
CO2	1	5000.35108	4.283E-25	8.718E	-6.0686	2004.66040		R 50
N2O	1	5000.42800	2.990E-23	6.004E	-7.0720	316.67001		P 27
CO2	2	5000.47617	3.192E-25	4.751E	-6.0816	754.88672		P 16
CO2	1	5000.48083	4.913E-22	9.496E	-6.0719	464.17169		R 34
CO2	2	5000.48693	5.953E-27	4.687E	-6.0720	1710.65918		P 32
H2O	1	5000.54070	6.959E-27	1.096E	-8.0557	1411.61206	9 5 4	8 6 3
H2O	4	5000.75000	4.629E-27	3.108E	-6.0857	809.39502	8 3 5	8 4 4
CO2	1	5000.83037	9.346E-26	8.702E	-6.0669	2340.73218		R 65
H2O	4	5000.83600	4.469E-26	3.439E	-6.0923	300.61700	5 0 5	6 1 6
CO2	2	5000.85697	7.714E-24	5.195E	-6.0856	60.87300		R 12
CO2	3	5000.99115	2.146E-26	1.502E	-6.0704	930.09857		P 50

FIGURE 23 Example of data contained within the HITRAN database showing individual absorption lines, frequency, line intensity, and other spectroscopic parameters.
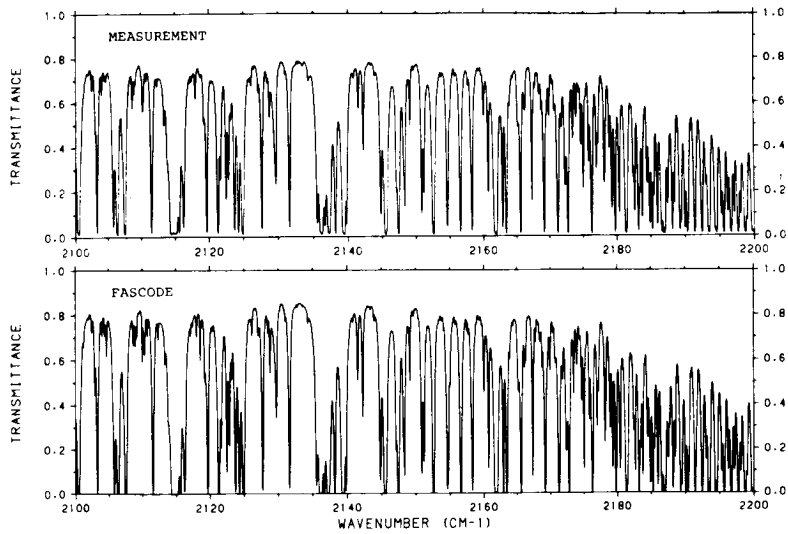
FIGURE 24 Comparison of an FASCOD2 transmittance calculation with an experimental atmospheric measurement (from NRL) over a 6.4-km path at the ground. *(Courtesy of S. Clough, Ref. 23.)*

interval of $350 \, cm^{-1}$ to $40{,}000 \, cm^{-1}$ (i.e., 250-nm to 28-μm wavelength). The spectral range of the LOWTRAN program extends into the UV. In the LOWTRAN program, the total transmittance at a given wavelength is given as the product of the transmittances due to molecular band absorption, molecular scattering, aerosol extinction, and molecular continuum absorption. The molecular band absorption is composed of four components of water vapor, ozone, nitric acid, and the uniformly mixed gases (CO_2, N_2O, CH_4, CO, O_2, and N_2).

The latest version of LOWTRAN (7) contains models treating solar and lunar scattered radiation, spherical refractive geometry, wind-dependent maritime aerosols, vertical structure aerosols, cirrus cloud model, and a rain model.[26] As an example, Fig. 25 shows a
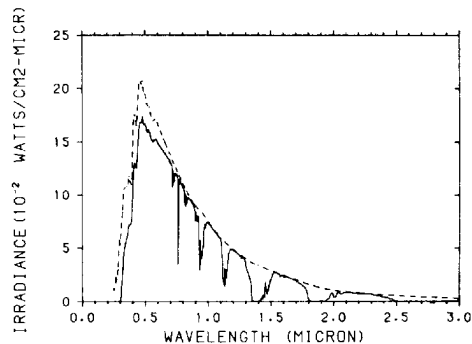

FIGURE 25 Solar radiance model (dashed line) and directly transmitted solar irradiance (solid line) for a vertical path, from the ground (U.S. standard 1962 model, no aerosol extinction) as used by the LOWTRAN program.
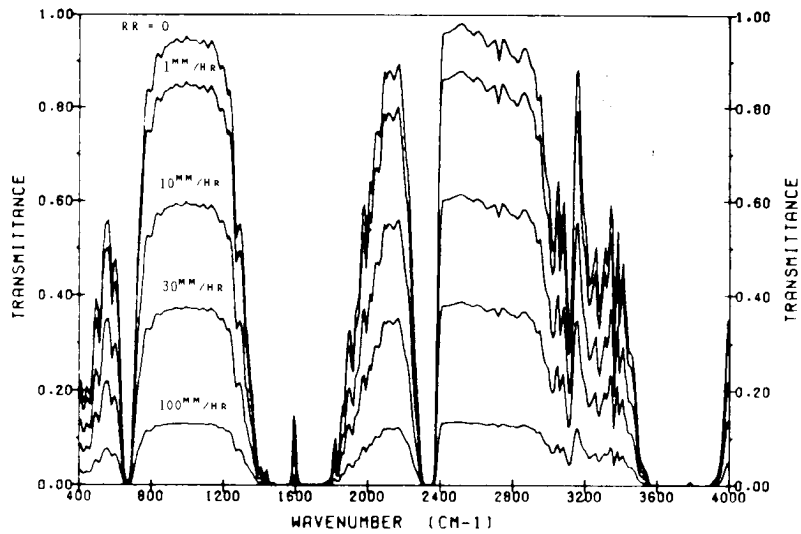
FIGURE 26 Atmospheric transmittance for different rain rates and for spectral frequencies from 400 to 4000 cm^{-1}. The measurement path is 300 m at the surface with $T = T_{dew} = 10°C$, with a meteorological range of 23 km in the absence of rain.

ground-level solar radiance model used by LOWTRAN, and Fig. 26 shows an example of a rain-rate model and its effect upon the transmission of the atmosphere as a function of rain rate in mm of water per hour.[26]

Extensive experimental measurements have been made to verify LOWTRAN calculations. Figure 27 shows a composite plot of the LOWTRAN-predicted transmittance and experimental data for a path length of 1.3 km at sea level.[3] As can be seen, the agreement is quite good. It is estimated that the LOWTRAN calculations are good to about
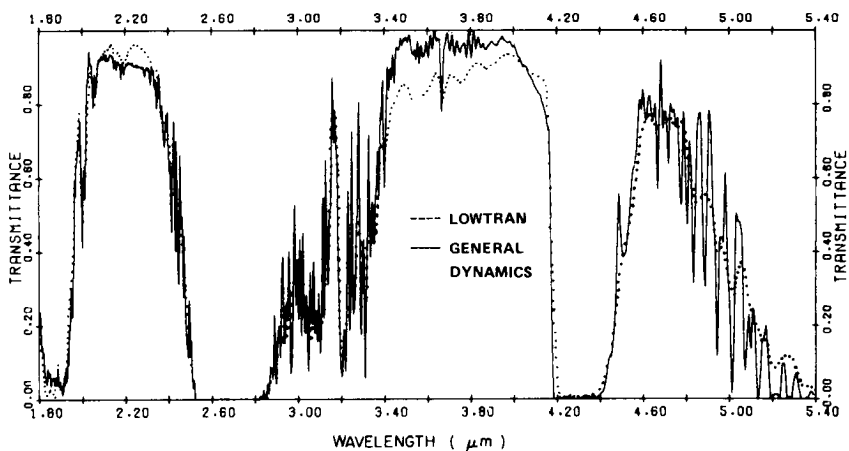

FIGURE 27 Comparison between LOWTRAN predicted spectrum and General Dynamics atmospheric measurements; range = 1.3 km at sea levels. *(From Ref. 3.)*

10 percent.[3] It should be added that the molecular absorption portion of the preceding LOWTRAN (moderate-resolution) spectra can also be generated using the high-resolution FASCODE/HITRAN program and then spectrally smoothing (i.e., degrading) the spectra to match that of the LOWTRAN spectra.

The most recent extension of the LOWTRAN program is the MODTRAN program. MODTRAN is similar to LOWTRAN but has increased spectral resolution. At present, the resolution for MODTRAN can be specified by the user between 2 and 20 cm^{-1}.

Programs and Databases for Use on Personal Computers

The preceding databases and computer programs have been converted or modified to run on different kinds of personal computers.[28,29] Currently, the HITRAN 1992 database can be obtained on CD-ROMs, and is also being offered as a random-access database which will fit on the hard disk drive of a personal computer (MS-DOS IBM-compatible computers). Several related programs are available, ranging from a complete copy of the FASCODE and LOWTRAN programs[28] to a simpler molecular transmission program of the atmosphere.[29] These programs calculate the transmission spectrum of the atmosphere and some show the overlay spectra of known laser lines. As an example, one version of these PC programs uses the HITRAN database and a transmission program to calculate the high-resolution spectrum of the atmosphere and displays the contribution of each individual molecule. Figure 28 shows the transmission spectrum produced by such a program.[29] The individual absorption lines are shown in the upper plot in Fig. 28 and the composite transmission is shown in the lower plot.

While these PC versions of the HITRAN database and transmission programs have become available only recently, they have already made a significant impact in the fields of atmospheric optics and optical remote sensing. They allow quick and easy access to atmospheric spectral data which was previously only available on a mainframe computer. It should be added that other computer programs are available which allow one to add or subtract different spectra generated by these HITRAN-based programs, from spectroscopic instrumentation such as FT-IR spectrometers or from other IR gas spectra databases. In the latter case, for example, the U.S. National Institute of Standards and Technology (NIST) has compiled a computer database of the qualitative IR absorption spectra of over 5200 different gases (toxic and other hydrocarbon compounds) with a spectral resolution of 4 cm^{-1}.[30] In addition, higher-resolution quantitative spectra for a limited group of gases can be obtained from several commercial companies.[30]

44.6   ATMOSPHERIC OPTICAL TURBULENCE

The most familiar effects of refractive turbulence in the atmosphere are the twinkling of stars and the shimmering of the horizon on a hot day. The first of these is a random fluctuation of the amplitude of light also known as scintillation. The second is a random fluctuation of the phase front that leads to a reduction in the resolution of an image. Other effects include the wander and break-up of an optical beam.

In the visible and near-IR region of the spectrum, the fluctuations of the refractive index in the atmosphere are determined by fluctuations of the temperature. These temperature fluctuations are caused by turbulent mixing of air of different temperatures. In the far-IR region, humidity fluctuations also contribute.
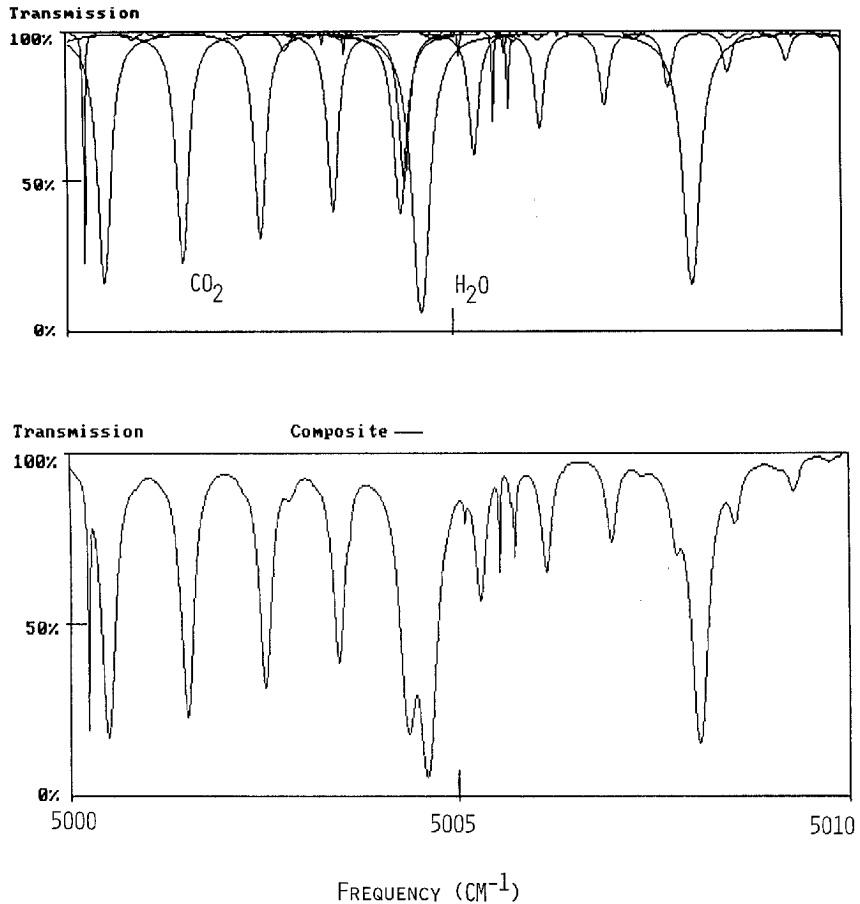
FIGURE 28 Example of generated atmospheric transmission spectrum obtained from HITRAN PC computer program showing individual molecular contribution and composite spectrum. *(From Ref. 29.)*

Turbulence Characteristics

Refractive turbulence in the atmosphere can be characterized by three parameters. The outer scale L_o is the length of the largest scales of turbulent eddies. The inner scale l_o is the length of the smallest scales. For eddies in the inertial subrange (sizes between the inner and outer scale), the refractive index fluctuations are best described by the structure function. This function is defined by

$$D_n(r_1, r_2) = \langle [n(r_1) - n(r_2)]^2 \rangle \tag{14}$$

where $n(r_1)$ is the index of refraction at point r_1 and the angle brackets denote an ensemble average. For homogeneous and isotropic turbulence it depends only on the distance between the two points r and is given by
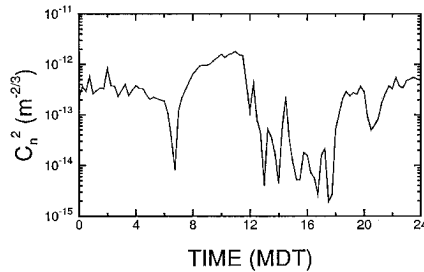
$$D_n(r) = C_n^2 r^{2/3} \tag{15}$$

FIGURE 29 Plot of refractive-turbulence structure parameter C_n^2 for a typical summer day near Boulder, Colorado. *(Courtesy G. R. Ochs, NOAA WPL.)*

where C_n^2 is a measure of the strength of turbulence and is defined by this equation.

In the boundary layer (the lowest few hundred meters of the atmosphere), turbulence is generated by radiative heating and cooling of the ground. During the day, solar heating of the ground drives convective plumes. Refractive turbulence is generated by the mixing of these warm plumes with the cooler air surrounding them. At night, the ground is cooled by radiation and the cooler air near the ground is mixed with warmer air higher up by winds. A period of extremely low turbulence exists at dawn and at dusk when there is no temperature gradient in the lower atmosphere. Turbulence levels are also very low when the sky is overcast and solar heating and radiative cooling rates are low. Measured values of turbulence strength near the ground vary from less than 10^{-17} to greater than 10^{-12} m$^{-2/3}$ at heights of 2 to 2.5 m.[31,32]

Figure 29 illustrates typical summertime values near Boulder, Colorado. This is a 24-hour plot of 15-minute averages of C_n^2 measured at a height of about 1.5 m on August 22, 1991. At night, the sky was clear, and C_n^2 was a few parts times 10^{-13}. The dawn minimum is seen as a very short period of low turbulence just after 6:00. After sunrise, C_n^2 increases rapidly to over 10^{-12}. Just before noon, cumulus clouds developed, and C_n^2 became lower with large fluctuations. At about 18:00, the clouds, dissipated, and turbulence levels increased. The dusk minimum is evident just after 20:00, and then turbulence strength returns to typical nighttime levels.

From a theory introduced by Monin and Obukhov,[33] a theoretical dependence of turbulence strength on height in the boundary layer above flat ground can be derived.[34,35] During periods of convection C_n^2 decreases as the $-4/3$ power of height. At other times (night or overcast days), the power is more nearly $-2/3$. These height dependencies have been verified by a number of experiments over relatively flat terrain.[36–40] However, values measured in mountainous regions are closer to the $-1/3$ power of height day or night.[41] Under certain conditions, the turbulence strength can be predicted from meteorological parameters and characteristics of the underlying surface.[42–44]

Farther from the ground, no theory for the turbulence profile exists. Measurements have been made from aircraft[31,36] and with balloons.[45–47] Profiles of C_n^2 have also been measured remotely from the ground using acoustic sounders,[48–50] radar,[36,37,51–56] and optical techniques.[46,57–60] The measurements show large variations in refractive turbulence strength. They all exhibit a sharply layered structure in which the turbulence appears in layers of the order of 100 m thick with relatively calm air in between. In some cases these layers can be associated with orographic features; that is, the turbulence can be attributed to mountain lee waves. Generally, as height increases, the turbulence decreases to a minimum value that occurs at a height of about 3 to 5 km. The turbulence level then increases to a maximum at about the tropopause (10 km). Turbulence levels decrease rapidly above the tropopause.

Model turbulence profiles have evolved from this type of measurement. Perhaps the best available model for altitudes of 3 to 20 km is the Hufnagel model:[61,62]

$$C_n^2 = \left\{ \left[(2.2 \times 10^{-53}) h^{10} \left(\frac{W}{27} \right)^2 \right] \exp\left(-\frac{h}{1000} \right) + 10^{-16} \exp\left(-\frac{h}{1500} \right) \right\} \exp\left[u(h, t) \right] \quad (16)$$

where h is the height above sea level in meters, W is the vertical average of the square of the wind speed, and u is a random variable that allows the random nature of the profiles to be modeled. W is defined by

$$W^2 = \frac{1}{1500} \int_{5000}^{20,000} v^2(h) \, dh \quad (17)$$

where $v(h)$ is the wind speed at height h. In data taken over Maryland, W was normally distributed with a mean value of 27 m/s and a standard deviation of 9 m/s. The random variable u is assumed to be a zero-mean, gaussian variable with a covariance function given by

$$\langle u(h, t) u(h + \delta h, t + \delta t) \rangle = A(\delta h/100) \exp\left(-\delta t/5 \right) + A(\delta h/2000) \exp\left(-\delta t/80 \right) \quad (18)$$

where

$$A(\delta h/L) = 1 - |\delta h/L|, \qquad \text{for} \qquad |h| < L \quad (19)$$

and equals 0 otherwise.

The time interval δt is measured in minutes. The average C_n^2 profile can be found by recognizing that $\langle \exp(u) \rangle = \exp(1)$. To extend the model to local ground level, one should add the surface layer dependence (e.g., $h^{-4/3}$ for daytime).

Another attempt to extend the model to ground level is the Hufnagel-Valley model.[63] This is given by

$$C_n^2 = 0.00594 \left(\frac{W}{27} \right)^2 (h \times 10^{-5})^{10} \exp\left(-\frac{h}{1000} \right) + 2.7 \times 10^{-16} \exp\left(-\frac{h}{1500} \right) + A \exp\left(-\frac{h}{100} \right)$$
$$(20)$$

Where W is commonly set to 21 and A to 1.7×10^{-14}. This specific model is referred to as the $HV_{5/7}$ model because it produces a coherence diameter r_0 of about 5 cm and an isoplanatic angle of about 7 µrad for a wavelength of 0.5 µm. Although this is not as accurate for modeling turbulence near the ground, it has the advantage that the moments of the turbulence profile important to propagation can be evaluated analytically.[63]

The $HV_{5/7}$ model is plotted as a function of height in the dashed line in Fig. 30. The solid line in the figure is a balloon measurement taken in College Station, Pennsylvania. The data were reported with 20-m vertical resolution and smoothed with a gaussian filter with a 100-m $\exp(-1)$ full-width. This particular data set was chosen because it has a coherence diameter of about 5 cm and an isoplanatic angle of about 7 µrad. The layered structure of the real atmosphere is clear in the data. Note also the difference between the model atmosphere and the real atmosphere even when the coherence diameter and the isoplanatic angle are similar.

Less is known about the vertical profiles of inner and outer scales. Near the ground (1 to 2 m) we typically observe inner scales of 5 to 10 mm over flat grassland in Colorado. Calculations of inner scale from measured values of Kolmogorov microscale range from 0.5 to 9 mm at similar heights.[64] Aircraft measurements of dissipation rate were used along with a viscosity profile calculated from typical profiles of temperature and pressure to estimate a profile of microscale.[65] Values increase monotonically to about 4 cm at a height of 10 km and to about 8 cm at 20 km.
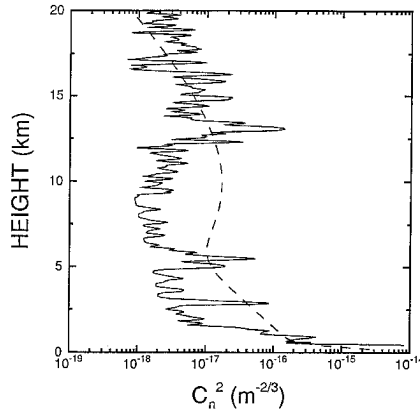
FIGURE 30   Turbulence strength C_n^2 as a function of height. The solid line is a balloon measurement made in College Station, Pennsylvania, and the dashed line is the $HV_{5/7}$ model. *(Courtesy R. R. Beland, Geophysics Directorate, Phillips Laboratory, U.S. Air Force.)*

Near the ground, the outer scale can be estimated using Monin-Obukhov similarity theory.[33] The outer scale can be defined as that separation at which the structure function of temperature fluctuations is equal to twice the variance. Using typical surface layer scaling relationships[66] we see that

$$L_0 = \begin{cases} 7.04h(1 - 7S_{MO})(1 - 16S_{MO})^{-3/2} & \text{for} \quad -2 < S_{MO} < 0 \\ 7.04h(1 + S_{MO})^{-3}(1 + 2.75S_{MO}^{2/3})^{-3/2} & \text{for} \quad 0 < S_{MO} < 1 \end{cases} \tag{21}$$

where S_{MO} is the Monin-Obukhov stability parameter. For typical daytime conditions ($S_{MO} < 0$), L_o is generally between $h/2$ and h.

Above the boundary layer, the situation is more complex. Weinstock[67] calculated that L_o should be about 330 m in moderate turbulence in the stratosphere. Barat and Bertin[68] measured outer scale values of 10 to 100 m in a turbulent layer using a balloon-borne instrument. Some recent optical data[69,70] suggest that the outer scale is generally smaller with a peak value of about 4 m at a height of 8.5 km. Other data[71] supply no evidence for an outer scale less than about 1 km. These results are still controversial and more measurements of outer scale are needed to resolve the issue.

Beam Wander

The first effect of refractive turbulence to consider is the wander of an optical beam in the atmosphere. The deviations of the centroid of a beam in each of the two orthogonal transverse axes will be independent gaussian random variables. This wander is generally characterized statistically by the variance of the angular displacement. In isotropic turbulence, the variances in the two axes are equal and the magnitude of the displacement is a Rayleigh random variable with a variance that is twice that of the displacement in a single axis. Both the single-axis and the magnitude variances are reported in the literature.

Three main approaches to the calculation of beam-wander variance have been used. (1) If diffraction effects are negligible and if the path-integrated turbulence is small enough, the geometric optics approximation[72–75] can be used. Diffraction effects are negligible

when the aperture diameter is greater than the Fresnel zone size.[75] The other condition requires that the product of the transverse coherence of the field and the aperture diameter is greater than the square of the Fresnel zone size.[75] (2) If diffraction must be considered, the Huygens-Fresnel approximation[76–79] can be used. (3) The most complete theory uses the Markov random process approximation to the moment equation.[80–82] In the two types of calculation that include diffraction, beams with a gaussian irradiance profile are generally assumed.

In the geometric optics approximation, the variance of the angular displacement in a single axis is given by[75]

$$\sigma_d^2 = 2.92 D^{-1/3} \int_0^L dz C_n^2(z) \frac{\left(1 - \dfrac{z}{L}\right)^2}{\left|1 - \dfrac{z}{F}\right|^{1/3}} \tag{22}$$

where D is the diameter of the initial beam, z is position along the path, L is the propagation path length, and F is the geometric focal range of the initial beam (negative for a diverging beam). For homogeneous turbulence and a beam that does not come to a focus between the transmitter and observation plane, Eq. (22) reduces to

$$\sigma_d^2 = 0.97 C_n^2 D^{-1/3} L {}_2F_1\left(\tfrac{1}{3}, 1; 4; \frac{L}{F}\right) \tag{23}$$

where ${}_2F_1$ is the hypergeometric function. The hypergeometric function is 1 for a collimated beam and 1.125 for a focused beam.

In the Markov approximation, the single-axis variance is given by[80]

$$\sigma_d^2 = 4\pi^2 \int_0^L dz \left(1 - \frac{z}{L}\right)^2 \int_0^\infty dK K^3 \Phi_n(K, z)$$
$$\times \exp\left\{ -\frac{K^2 D^2}{8}\left[\left(1 - \frac{z}{F}\right)^2 + \frac{16 z^2}{K^2 D^4}\right] - \pi D_\Psi\left(\frac{Kz}{k}\right)\right\} \tag{24}$$

where $\Phi_n(K, z)$ is the path-dependent refractive index spectrum, K is the wave number of turbulence, D is the $\exp(-1)$ intensity diameter of the initial beam, k is the optical wave number, and $D_\Psi(\rho)$ is the wave structure function for separation ρ of a spherical wave. The structure function is given by

$$D_\Psi(\rho) = 8\pi^2 k^2 \int_0^z dz' \int_0^\infty dK' K' \Phi_n(K', z')[1 - J_0(K'\rho z'/z)], \tag{25}$$

where J_0 is the zero-order Bessel function of the first kind. The last term in the exponential of Eq. (24) is a correction term for strong turbulence. The middle term includes the effects of diffraction.

Beam Spreading

The next effect of refractive turbulence to consider is the spread of an optical beam as it propagates through the atmosphere. There are two types of beam spread denoted as long-term and short-term. The long-term beam spread is defined as the turbulence-induced beam spread observed over a long time average. It includes the effects of the slow wander of the entire beam. The short-term beam spread is defined as the beam spread observed at an instant of time. It does not include the effects of beam wander and is often approximated by the long-term beam spread with the effects of wander removed, although the two are not identical.

We can consider beam wander to be caused by turbulent eddies that are larger than the beam. Short-term beam spread is caused by turbulent eddies that are smaller than the beam. There are more small eddies than large in the beam at any time which implies that the beam spread at any instant is averaged over more eddies. As a result, the fluctuations of short-term beam spread are much smaller than those of beam wander and are typically neglected. The primary effect of short-term beam spread is to spread the average energy over a larger area. Thus, the average value of the on-axis irradiance is reduced, and the average value of the irradiance at large angles is increased.

The extended Huygens-Fresnel principle can be used to calculate the long-term spread of a gaussian beam in refractive turbulence.[83–87] The $\exp(-1)$ intensity radius of a gaussian beam is

$$p_1 = \left[\frac{4}{k^2 D^2} + \frac{D^2}{4}\left(1 - \frac{L}{F}\right)^2 + \frac{4}{k^2 \rho_0^2} \right]^{1/2} \tag{26}$$

where D is the $\exp(-1)$ intensity diameter of the source and ρ_o is the phase coherence length that would be observed for a point source propagating from the receiver to the transmitter. The first term in this equation is the diffraction beam spread, the second is the geometrical optics projection of the transmitter aperture, and the final term is the total turbulence-induced spread.

The phase coherence length is defined as the transverse separation at which the coherence of the field is reduced to $\exp(-1)$. If the coherence length ρ_o is much larger than the inner scale, the structure function is given by $D_\Psi(\rho) = 2(\rho/\rho_o)^{5/3}$ and

$$\rho_o = \left[1.46 k^2 \int_0^L dz \left(\frac{z}{L}\right)^{5/3} C_n^2(z) \right]^{-3/5} \tag{27}$$

If the coherence length is much smaller than the inner scale, then $D_\Psi(\rho) = 2(\rho/\rho_o)^2$ and

$$\rho_o = \left[1.86 k^2 \int_0^L dz \left(\frac{z}{L}\right)^2 C_n^2(z) l_o^{-1/3}(z) \right]^{-1/2} \tag{28}$$

Typical values of p_o for spherical-wave propagation through homogeneous turbulence are presented in Fig. 31. In these plots there is a slope change from $L^{-3/5}$ to $L^{-1/2}$ where p_o
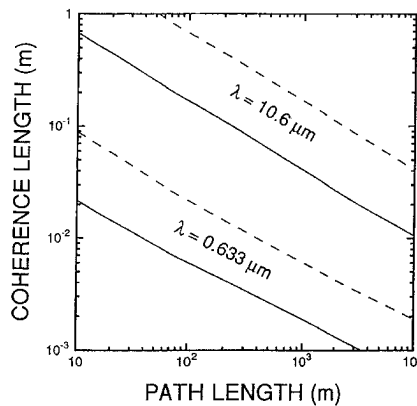

FIGURE 31   Coherence length ρ_o as a function of path length for two common laser wavelengths. An inner scale of 1 cm, and values of 10^{-12} (solid lines) and 10^{-13} (dashed lines) were used in the calculations.

is about equal to the inner scale of 1 cm. This small change is nearly imperceptible in the figure.

The extended Huygens-Fresnel principle has been used to calculate the short-term beam spread by explicitly subtacting the beam wander.[88–91] If p_o and l_o are much smaller than D, then the short-term beam spread is approximately given by

$$p_s = \left\{ \frac{4}{k^2 D^2} + \frac{D^2}{4L^2} \left(1 - \frac{L}{F} \right)^2 + \frac{4}{k^2 \rho_0^2} \left[1 - 0.62 \left(\frac{\rho_o}{D} \right)^{1/3} \right]^{6/5} \right\}^{1/2} \tag{29}$$

If ρ_o is much greater than D, the turbulence-induced component of beam spreading can be neglected.

If inner scale and outer scale effects are included, more complicated integral expressions result.[92] Numerical calculations were performed for truncated gaussian beams with central obscurations.[93] The following approximation was obtained by a curve fit to the results:

$$p_s = \left(1 + 0.182 \frac{D_{\text{eff}}^2}{r_o^2} \right)^{1/2} p_d \qquad \text{for} \qquad \frac{D_{\text{eff}}}{r_o} < 3$$

$$p_s = \left[1 + \left(\frac{D_{\text{eff}}}{r_o} \right)^2 - 1.18 \left(\frac{D_{\text{eff}}}{r_o} \right)^{-5/3} \right]^{1/2} p_d \qquad \text{for} \qquad 3 < \frac{D_{\text{eff}}}{r_o} < 7.5 \tag{30}$$

where D_{eff} is the effective diameter of the truncated aperture, $r_o = 2.099\, p_o$, and p_d is the diffraction-limited value. These expressions agree fairly well with available data.[78,94,95]

Imaging and Heterodyne Detection

The problem of imaging through the turbulent atmosphere is similar to the problem of beam propagation through the atmosphere. The dancing of an image in the focal plane of an imaging system is mathematically equivalent to the wander of a beam focused at the object by the same optical system. The resolution of the short-exposure image is equivalent to the short-term beam spread of the same focused beam. The resolution for a long exposure is related to the long-term beam spread.

Thus, the position of the image of a point object will drift in each axis in the focal plane. The variance of that drift is given by[96]

$$\sigma_i^2 = 1.10 C_n^2 D^{-1/3} L F^2 \tag{31}$$

where D is the aperture diameter of the imaging system, F is its focal length, and L is the distance to the object.

Fried[97] used the idea of tilt correction to calculate the average image resolution for a short-exposure image in the turbulent atmosphere. This problem is mathematically equivalent to the propagation of a beam in the opposite direction if the imaging aperture replaces the beam width. These results were refined by Lutomirski et al.[98] and applied to a space-to-ground path by Valley.[92]

Image resolution is also related to the signal-to-noise ratio of an optical heterodyne receiver. The long-exposure resolution is equivalent to a staring receiver. The short-exposure resolution is equivalent to a receiver that employs tilt-correction of the signal or of the local oscillator.[97,99–101]

Scintillation

The refractive index inhomogeneities that distort the optical phase front also produce amplitude scintillation at some distance. The first cases to be considered were plane-wave and spherical-wave propagation through weak path-integrated turbulence where the weak-turbulence condition requires that fluctuations of irradiance be much less than the mean value. Tatarskii[102] used a perturbation approach to the wave equation. Lee and Harp[103] used a physical approach to arrive at the same results. These results are summarized in a number of good reviews.[90,91,104,105]

We will first consider the weak-turbulence results. For propagation from space to the ground, the plane wave formula is generally valid. The variance of irradiance fluctuations (normalized by the mean irradiance value) is given by[104]

$$\sigma_r^2 = k^{7/6} \sec^{11/6} \theta \int_0^\infty dh h^{5/6} C_n^2(h) \tag{32}$$

where k is the optical wave number, θ is the zenith angle, and h is the height of the receiver above the ground. This expression is valid as long as the path-integrated turbulence is weak enough that the variance is much less than unity. This condition is usually met for near-zenith propagation.

For propagation of diverging waves near the ground, the spherical-wave approximation is often valid. Assuming constant turbulence along the path, the weak-turbulence variance in this case is given by[104]

$$\sigma_r^2 = \exp\left[0.5 k^{7/6} L^{11/6} C_n^2\right] - 1 \qquad \text{for} \qquad l_o < \sqrt{\lambda L}$$

$$\sigma_r^2 = \exp\left[1.28 L^3 l_o^{-7/3} C_n^2\right] - 1 \qquad \text{for} \qquad l_o > \sqrt{\lambda L} \tag{33}$$

where L is the path length and l_o is the inner scale of turbulence.

For narrow-beam propagation, the effects of the finite beam must be considered. Kon and Tatarskii[106] calculated the amplitude fluctuations of a collimated beam using the perturbation technique. Schmeltzer[107] extended these results to include focused beams. These results were used to obtain numerical values for a variety of propagation conditions.[108–110] Ishimaru[111–113] used a spectral representation to obtain similar results. Under certain conditions, one sees a reduction in the variance on the optical axis[108,109,114,115] and an increase off of the optical axis.[116]

The spatial scale of weak scintillations is about equal to the larger of either the Fresnel zone size $(L/k)^{1/2}$ or the inner scale.[104] Scintillation will be reduced if an aperture larger than the scale size is used to collect the light. If the aperture diameter D is much larger than the scale size, the reduction factor can be expressed as[117,118]

$$A = C\left(\frac{D}{D_0}\right)^{-7/3} \tag{34}$$

where D_0 is $(\lambda L)^{1/2}$ and C is 4.71 for a plane wave and 23.5 for a spherical wave when the inner scale is much smaller than the Fresnel zone. If the inner scale is much larger than the Fresnel zone, D_0 is the inner scale and C is 0.45 for a plane wave and 9.17 for a spherical wave.

It is generally accepted that the probability density function for weak scintillation is log normal.[90,102,104,119] This density function has the form

$$p(I) = \frac{1}{\sqrt{2\pi}\,\sigma_I I} \exp\left[-\frac{1}{2\sigma_r^2}(\ln I + 0.5\sigma_r^2)^2\right] \tag{35}$$

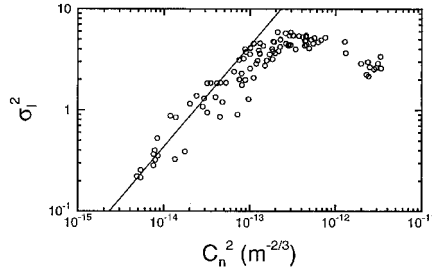**FIGURE 32** Plot of normalized variance of irradiance σ_I^2 as a function of turbulence strength C_n^2. Circles are data taken with a 488-nm wavelength laser over a 1200-m path, and the line is the corresponding weak-turbulence theory.

The weak-turbulence theory is, in essence, a single-scattering theory. As the path-integrated turbulence becomes larger, multiple-scattering effects become important, and this theory breaks down. Actual observed values of irradiance variance are smaller than predicted in this region as shown in Fig. 32. The circles in this figure are one-minute averages of irradiance variance for 488-nm laser light propagated across 1200 m of flat grassland. The solid line is the weak-turbulence approximation.

In these and other experiments, variance values reach a peak value of between 3 and 5 for a spherical wave and they begin to decrease with increasing turbulence strength.[120–123] In the limit of infinite path-integrated turbulence, the normalized variance of irradiance is predicted to approach unity.[124,125] In the intermediate region near the peak irradiance, numerical evaluation of currently available theories is impractical.

An asymptotic theory has been developed for very large path-integrated turbulence.[125–129] We assume that the inner scale is much less than the Fresnel zone in this regime because long paths are necessary to obtain large values of path-integrated turbulence. Then the irradiance variance can be approximated by

$$
\begin{aligned}
\sigma_r^2 &= 1 + 1.9\sigma_R^{-4/5} &&\text{for spherical waves} \\
\sigma_r^2 &= 1 + 0.86\sigma_R^{-4/5} &&\text{for plane waves}
\end{aligned}
\tag{36}
$$

where σ_R^2 is the appropriate (spherical-wave or plane-wave) variance calculated from the Rytov approximation given by Eq. (32) or (33).

In very strong turbulence two distinct spatial scales are evident in the scintillation pattern.[125–129] The smaller scale is about the size of the coherence length ρ_o discussed under "Beam Spreading." The larger scale is the size of the scattering disk which is the ratio of the square of the Fresnel zone to the coherence length ($L/k\rho_o$). As turbulence increases, the small scale becomes smaller and the large scale becomes larger. The strength of the small-scale fluctuations is constant in this regime and contributes a value of unity to the variance. The large-scale fluctuations contribute the rest of the variance and become weaker with increasing turbulence strength.

At high turbulence values, the density function is a log-normally modulated exponential.[123,130] This density function has the form

$$
p(I) = \frac{1}{\sqrt{2\pi}\,\sigma_z} \int_0^\infty \frac{dz}{z^2} \exp\left[-\frac{I}{z} - \frac{(\ln z + \frac{1}{2}\sigma_z^2)^2}{2\sigma_z^2} \right]
\tag{37}
$$

where the parameter σ_z^2 is related to the irradiance variance by the relationship

$$
\sigma_I^2 = 2\exp(\sigma_z^2) - 1
\tag{38}
$$

An interesting feature of this density function is that the most likely value of the irradiance is 0. Although the observed signal is occasionally very bright, quite often there is no signal unless some sort of averaging is performed.

44.7 *EXAMPLES OF ATMOSPHERIC OPTICAL REMOTE SENSING*

One of the more important applications of atmospheric optics is optical remote sensing. Atmospheric optical remote sensing concerns the use of an optical or laser beam to remotely sense information about the atmosphere or a distant target. Optical remote sensing measurements are diverse in nature and include the use of a spectral radiometer aboard a satellite for the detection of trace species in the upper atmosphere, the use of spectral emission and absorption from the earth for the detection of the concentration of water vapor in the atmosphere, the use of lasers to measure the range-resolved distribution of several molecules including ozone in the atmosphere, and Doppler wind measurements. In this section, some typical optical remote sensing experiments will be presented in order to give a flavor of the wide variety of atmospheric optical measurements that are currently being conducted. More in-depth references can be found in several current journal papers and conference proceedings.[131–136]

The Upper Atmospheric Research Satellite (UARS) was placed into orbit in September 1991 as part of the Earth Observing System. One of the optical remote sensing instruments aboard UARS is the High Resolution Doppler Imager (HRDI) developed by P. Hays' and V. Abreu's group at the University of Michigan.[137] The HRDI is a triple etalon Fabry-Perot Interferometer designed to measure Doppler shifts of molecular absorption and emission lines in the earth's atmosphere in order to determine the wind velocity of the atmosphere. A wind velocity of 10 m/s causes a Doppler shift of 2×10^{-5} nm for the oxygen lines detected near a wavelength of 600–800 nm. A schematic of the instrument is given in Fig. 33*a* which shows the telescope, triple Fabry-Perots, and unique imaging Photo-Multiplier tubes to detect the Fabry-Perot patterns of the spectral absorption lines. The HRDI instrument is a passive remote sensing system and uses the reflected or scattered sunlight as its illumination source. Figure 33*b* shows the wind field measured by UARS (HRDI) for an altitude of 90 km.

Another kind of atmospheric remote sensing instrument is represented by an airborne laser radar (lidar) system operated by E. Browell's group at NASA/Langley.[138] Their system consists of two pulsed, visible-wavelength dye laser systems that emit short (10-ns) pulses of tunable optical radiation that can be directed toward aerosol clouds in the atmosphere. By the proper tuning of the wavelength of these lasers, the difference in the absorption due to ozone, water vapor, or oxygen in the atmosphere can be measured. Because the laser pulse is short, the timing out to the aerosol scatterers can be determined and range-resolved lidar measurements can be made. Figure 34 shows range-resolved lidar backscatter profiles obtained as a function of the lidar aircraft ground position. The variation in the atmospheric density and ozone distribution as a function of altitude and distance is readily observed.

A Coherent Doppler Lidar is one which is able to measure the Doppler shift of the backscattered lidar returns from the atmosphere. Several Doppler lidar systems have been developed which can determine wind speed with an accuracy of 0.1 m/s at ranges of up to 15 km. One such system is operated by M. Hardesty's group at NOAA/WPL for the mapping of winds near airports and for meteorological studies.[139] Figure 35 shows a two-dimensional plot of the measured wind velocity obtained during the approach of a wind gust front associated with colliding thunderstorms; the upper figure shows the real-time Doppler lidar display of the measured radial wind velocity, and the lower plot shows the computed wind velocity. As seen, a Doppler lidar system is able to remotely measure the wind speed with spatial resolution on the order of 100 m. A similar Doppler
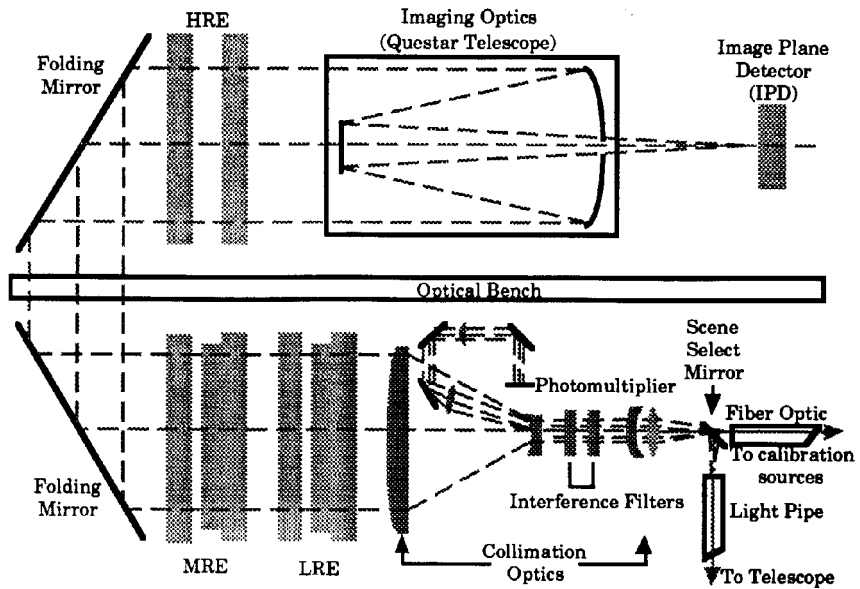
FIGURE 33 (*a*) Optical layout of the Upper Atmospheric Satellite (UARS) High Resolution Doppler Imager (HRDI) instrument. F.O. = fiber optic, LRE = low-resolution etalon, MRE = medium-resolution etalon, HRE = high-resolution etalon. *(From Hays, Ref. 137.)*
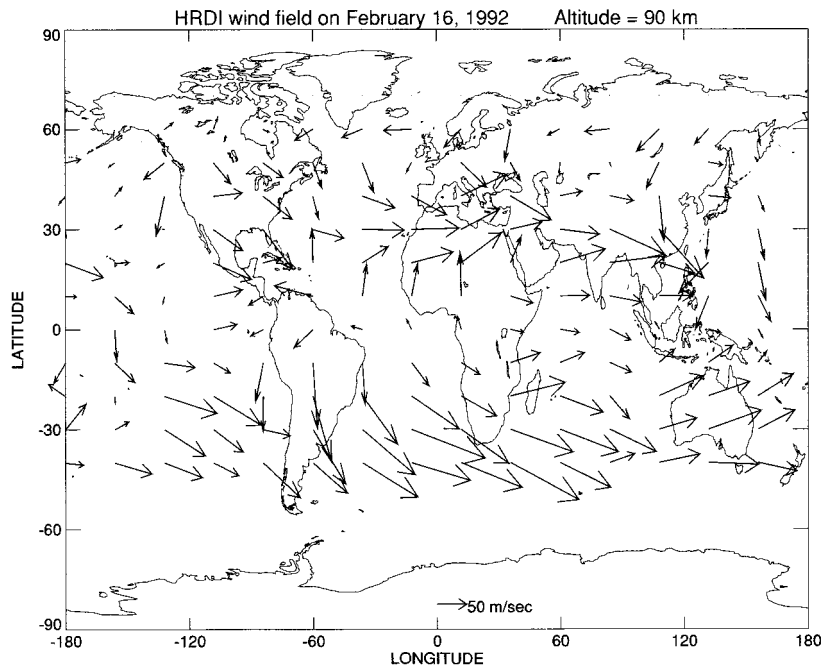

FIGURE 33 (*b*) Upper atmospheric wind field measured by UARS/HRDI satellite instrument. *(From Hays, Ref. 137.)*
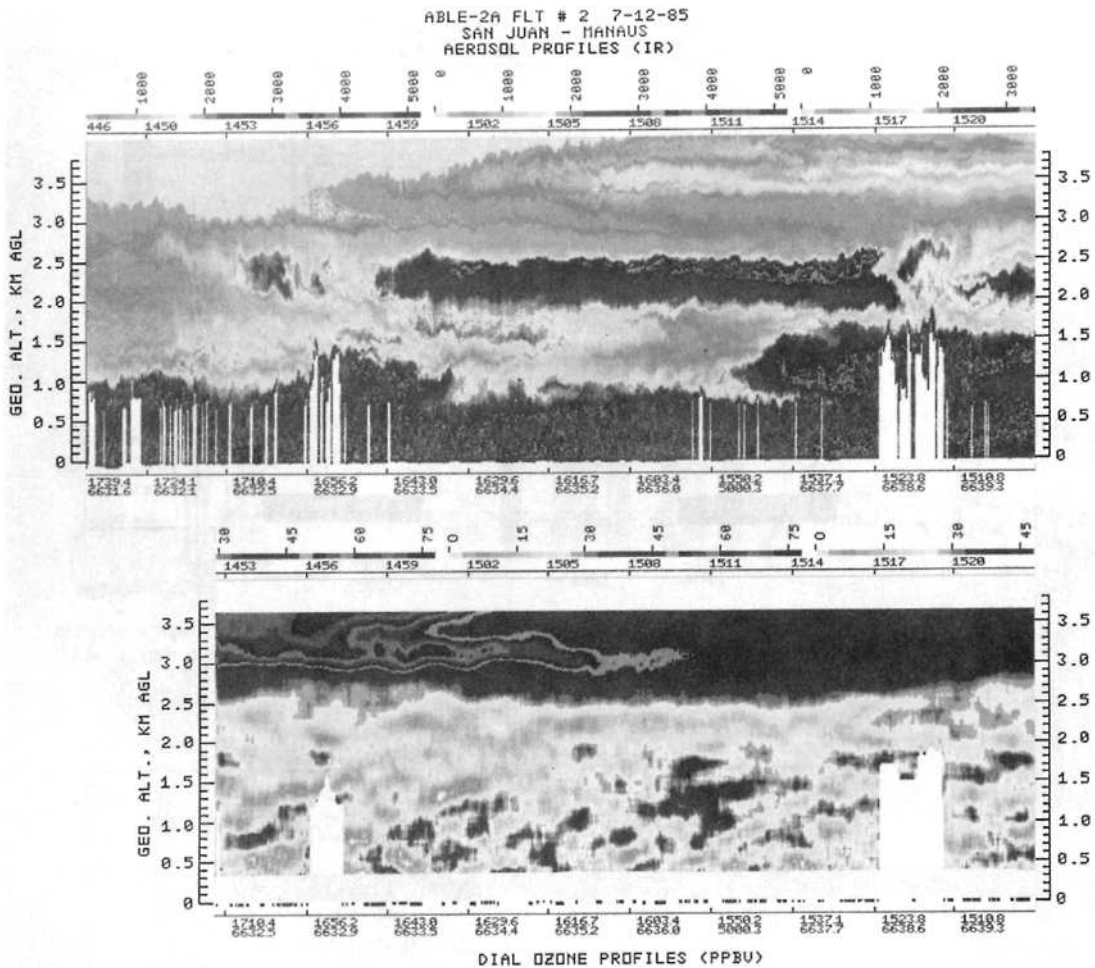
ABLE-2A FLT # 2 7-12-85
SAN JUAN - MANAUS
AEROSOL PROFILES (IR)

FIGURE 34   Range-resolved lidar measurements of atmospheric aerosols and ozone density. *(From E. Browell, Ref. 138.)*

lidar system is being considered for the early detection of windshear in front of commercial aircraft.

A further example of atmospheric optical remote sensing is that of the remote measurement of the global concentration and distribution of atmospheric aerosols and particulates. P. McCormick's group at NASA/Langley has developed the SAGE II satellite system which is part of a package of instruments to detect global aerosol and selected species concentrations in the atmosphere.[140] This system measures the difference in the optical radiation emitted from the earth's surface and the differential absorption due to known absorption lines or spectral bands of several species in the atmosphere, including ozone. The instrument also provides for the spatial mapping of the concentration of aerosols and particulates in the atmosphere, and an example of such a measurement is shown in Fig. 36. This figure shows the measured concentration of aerosols and particulates after the eruption of Mt. Pinatubo and demonstrates the global circulation and transport of the injected material into the earth's atmosphere.
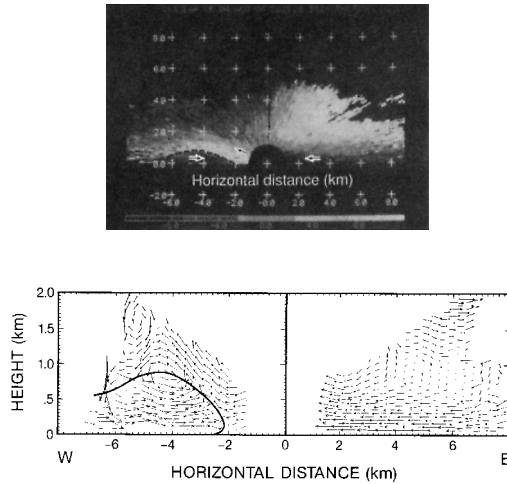
FIGURE 35 Coherent Doppler lidar measurements of atmospheric winds showing velocity profile of gust front. Upper plot is real-time display of Doppler signal and lower plot is range-resolved wind field. *(From M. Hardesty, Ref. 139.)*

The preceding examples are just a few of many different optical remote sensing instruments that are being used to measure the physical dynamics and chemical properties of the atmosphere. As is evident in these examples, an understanding of atmospheric optics plays an important and integral part in these measurements.

44.8 METEOROLOGICAL OPTICS

One of the most colorful aspects of atmospheric optics is that associated with meteorological optics. Meteorological optics involves the interplay of light with the atmosphere and the physical origin of the observed optical phenomena. Several excellent books have been written about this subject, and the reader should consult these and the contained references.[141,142] While it is beyond the scope of this chapter to present an overview of meteorological optics, some specific optical phenomena will be described to give the reader a sampling of some of the interesting effects involved in naturally occurring atmospheric and meteorological optics.

Some of the more common and interesting meteorological optical phenomena involve rainbows, ice-crystal halos, and mirages. The rainbow in the atmosphere is caused by internal reflection and refraction of sunlight by water droplets in the atmosphere. Figure 37 shows the geometry involved in the formation of a rainbow, including both the primary and larger secondary rainbow. Because of the dispersion of light within the water droplet, the colors or wavelengths are separated in the backscattered image. Although rainbows are commonly observed in the visible, such refraction also occurs in the infrared spectrum. As an example, Fig. 38 shows a natural rainbow in the atmosphere photographed with IR-sensitive film by R. Greenler.[142]

The phenomena of halos, arcs, and spots are due to the refraction of light by ice crystals suspended in the atmosphere. Figure 39 shows a photograph of collected ice crystals as
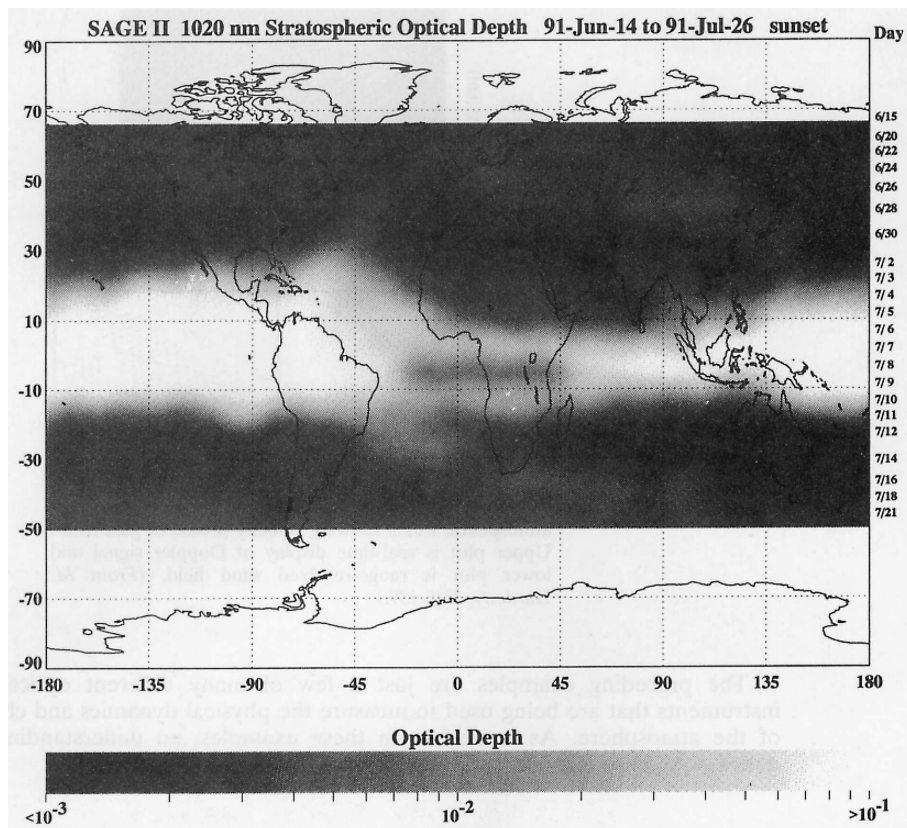
FIGURE 36 Measurement of global aerosol and particulate concentration using SAGE II satellite following eruption of Mt. Pinatubo. *(From P. McCormick, Ref. 140.)*

they fell from the sky. The geometrical shape, especially the hexagonal (six-sided) crystals, play an important role in the formation of halos and arcs in the atmosphere.

The common optical phenomenon of the mirage is caused by variation in the temperature and thus, the density of the air as a function of altitude or transverse geometrical distance. As an example, Fig. 40 shows the geometry of light-ray paths for a case where the air temperature decreases with height to a sufficient extent over the viewing angle that the difference in the index of refraction can cause a refraction of the image similar to total internal reflection. The heated air (less dense) near the ground can thus act like a mirror, and reflect the light upward toward the viewer. As an example, Fig. 41 shows a photograph taken by Greenler of motorcycles on a hot road surface. The reflected image of the motorcycles ''within'' the road surface is evident. There are many manifestations of mirages dependent upon the local temperature gradient and geometry of the situation. In many cases, partial and distorted images are observed leading to the almost surreal connotation often associated with mirages.

Finally, another atmospheric meteorological optical phenomenon is that of the green flash. A green flash is observed under certain conditions just as the sun is setting below the horizon. This phenomenon is easily understood as being due to the different relative displacement of each different wavelength or color in the sun's image due to spatially distributed refraction of the atmosphere.[142] As the sun sets, the last image to be observed
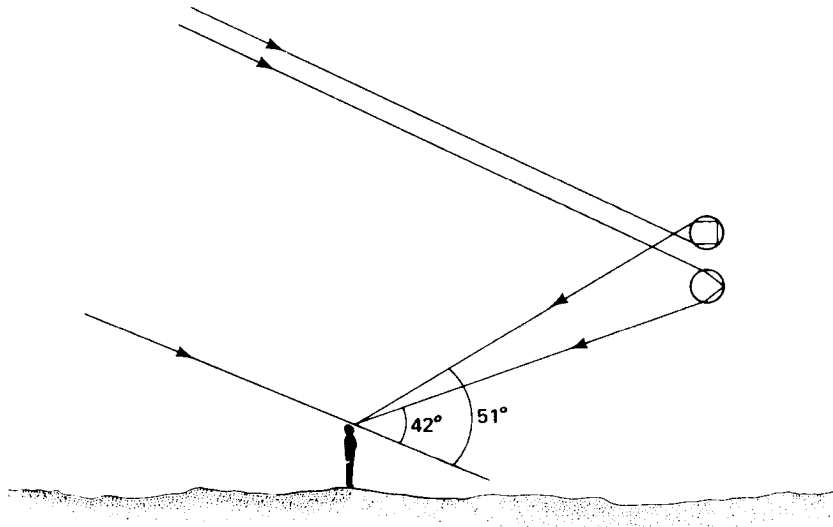
FIGURE 37 Different raindrops contribute to the primary and to the larger, secondary rainbow. *(From R. Greenler, Ref. 142.)*

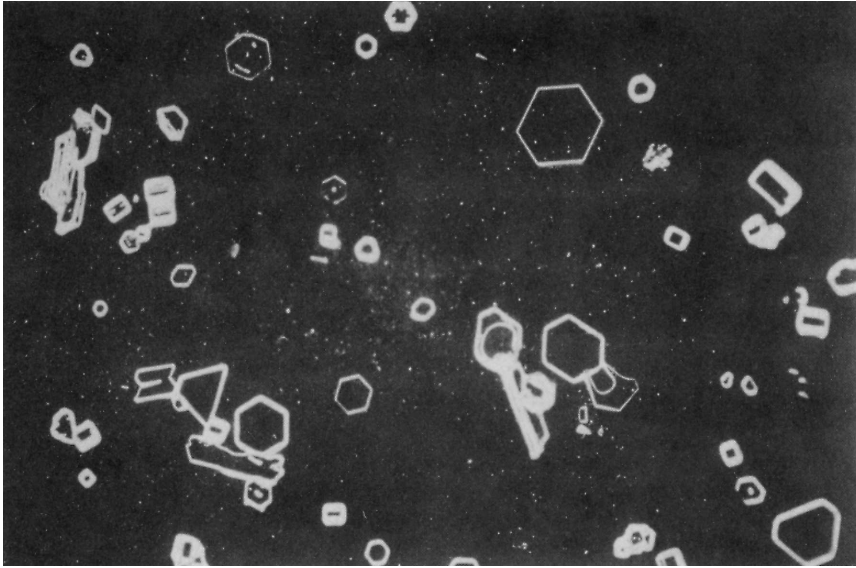**FIGURE 38** A natural infrared rainbow. *(Photograph courtesy of R. Greenler, Ref. 142.)*

FIGURE 39 Photograph of magnified small ice crystals collected as they fell from the sky. *(From R. Greenler, Ref. 142.)*
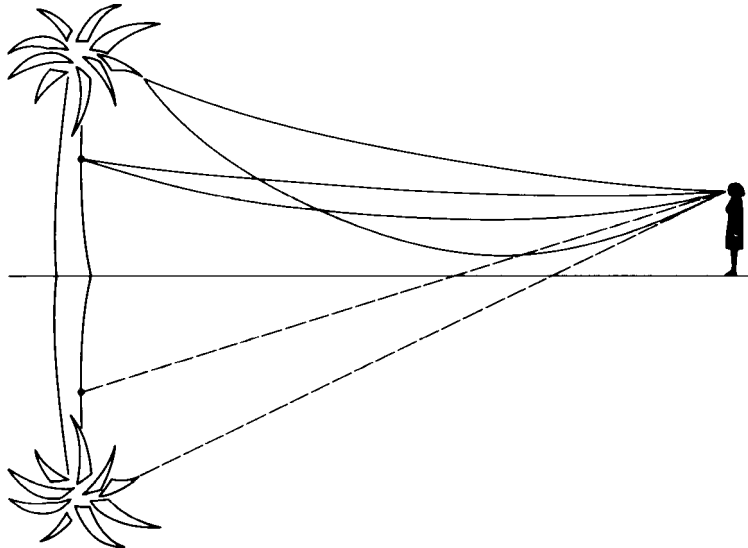

FIGURE 40 The origin of the inverted image in the desert mirage. *(From R. Greenler, Ref. 142.)*

FIGURE 41   The desert (or hot-road) mirage. In the inverted part of the image you can see the apparent reflection of motocycles, cars, painted stripes on the road, and the grassy road edge. *(From R. Greenler, Ref. 142.)*

is the shortest wavelength color, blue. However, most of the blue light has been Rayleigh scattered from the image seen by the observer so that the last image observed is closer to a green color. Under extremely clear atmospheric conditions when the Rayleigh scattering is not as preferential in scattering the blue light, the flash has been reported as blue in color.

44.9   ACKNOWLEDGMENTS

atmospheric optics from reading this chapter, and we encourage the reader to use the references cited for further in-depth study.

44.10   *REFERENCES*

1. R. M. Goody and Y. L. Young, *Atmospheric Radiation,* Oxford University Press, 1989.

2. W. G. Driscoll (ed.), Optical Society of America, *Handbook of Optics,* McGraw-Hill, 1978.

3. A. S. Jursa (sci. ed.), *Handbook of Geophysics and the Space Environment,* Air Force Geophysics Lab., NTIS Doc#ADA16700, 1985.

4. W. Wolfe and G. Zissis, *The Infrared Handbook,* Office of Naval Research, Wash. D.C., 1978.

5. R. Measures, *Laser Remote Sensing,* Wiley-Interscience, John Wiley & Sons, 1984.

6. "Major Concentration of Gases in the Atmosphere," NOAA S/T 76-1562, 1976; "AFGL Atmospheric Constituent Profiles (0–120 km)," AFGL-TR-86-0110, 1986; U.S. Standard Atmosphere, 1962 and 1976; Supplement 1966, U.S. Printing Office, Wash. D.C., 1976.

7. E. P. Shettle and R. W. Fenn, "Models of the Aerosols of the Lower Atmosphere and the Effects of Humidity Variations on Their Optical Properties," AFGL TR-79-0214; ADA 085951, 1979; A. Force, D. K. Killinger, W. DeFeo, and N. Menyuk, "Laser Remote Sensing of Atmospheric Ammonia Using a CO_2 Lidar System," *Appl. Opt.* **24:**2837 (1985); B. Nilsson, "Meteorological Influence on Aerosol Extinction in the 0.2–40 μm Range," *Appl. Opt.* **18:**3457 (1979).

8. J. F. Luhr, "Volcanic Shade Causes Cooling," *Nature* **354:**104 (1991).

9. L. S. Rothman, R. R. Gamache, A. Goldman, L. R. Brown, R. A. Toth, H. Pickett, R. Poynter, J. M. Flaud, C. Camy-Peyret, A. Barbe, N. Husson, C. P. Rinsland, and M. A. H. Smith, "The HITRAN Database: 1986 Edition," *Appl. Optics* **26:**4058 (1986); L. S. Rothman, R. R. Gamache, R. H. Tipping, C. P. Rinsland, M. A. H. Smith, D. C. Benner, V. Malathy Devi, J. M. Flaud, C. Camy-Peyret, A. Perrin, A. Goldman, S. T. Massie, L. R. Brown, and R. A. Toth, "The HITRAN Molecular Database: Editions of 1991 and 1992," *J. Quant. Spectrosc. Radiat. Transfer* **48:**469 (1992).

10. E. E. Whiting, "An Empirical Approximation to the Voigt Profile," *J. Quant. Spectrosc. Radiat. Transfer* **8:**1379 (1968); J. Olivero and R. Longbothum, "Empirical Fits to the Voigt Linewidth: A Brief Review," *J. Quant. Spectrosc. Radiat. Transfer* **17:**233 (1977); F. Schreir, "The Voigt and Complex Error Function—A Comparison of Computational Methods," *J. Quant. Spectrosc. Radiat. Transfer* **48:**734 (1992).

11. D. E. Burch, "Continuum absorption by H_2O," AFGL-TR-81-0300; ADA 112264, 1981; S. A. Clough, F. X. Kneizys, and R. W. Davies, "Lineshape and the Water Vapor Continuum," *Atmospheric Research* **23:**229 (1989).

12. Shardanand and A. D. Prasad Rao, "Absolute Rayleigh Scattering Cross Section of Gases and Freons of Stratospheric Interest in the Visible and Ultraviolet Region," NASA TN 0-8442 (1977); R. T. H. Collins and P. B. Russell, "Lidar Measurement of Particles and Gases by Elastic and Differential Absorption," in D. Hinkley (ed.), *Laser Monitoring of the Atmosphere,* Springer-Verlag, 1976.

13. E. U. Condon and H. Odishaw (eds.), *Handbook of Physics,* McGraw-Hill, 1967.

14. S. R. Pal and A. I. Carswell, "Polarization Properties of Lidar Backscattering from Clouds," *Appl. Opt.* **12:**1530 (1973).

15. G. Mie, "Bertrage Z. Phys. TruberMedien, Spezeziell kolloidaler Metallosungen," *Ann. Physik* **25:**377 (1908).

16. D. Deirnendjian, "Scattering and Polarization Properties of Water Clouds and Hazes in the Visible and Infrared," *Appl. Optics* **2:**187 (1964).

17. E. J. McCartney, *Optics of the Atmosphere,* Wiley, New York, 1976.

18. M. Wright, E. Proctor, L. Gasiorek, and E. Liston, ''A Preliminary Study of Air Pollution Measurement by Active Remote Sensing Techniques,'' NASA CR-132724, 1975.

19. P. McCormick and D. Winker, NASA/LaRC: 1 μm lidar measurement of aerosol distribution, private communication, 1991.

20. D. K. Killinger and N. Menyuk, ''Laser Remote Sensing of the Atmosphere,'' *Science* **235:**37 (1987).

21. R. W. Boyd, *Nonlinear Optics,* Academic Press, Orlando, Fla., 1992.

22. M. D. Levenson and S. Kano, *Introduction to Nonlinear Laser Spectroscopy,* Academic Press, Boston, 1988.

23. S. A. Clough, F. X. Kneizys, E. P. Shettle, and G. P. Anderson, ''Atmospheric Radiance and Transmittance: FASCOD2,'' *Proc. of Sixth Conf. on Atmospheric Radiation,* Williamsburg, Va., published by Am. Meteorol. Soc., Boston, 1986; J. A. Dowling, W. O. Gallery, and S. G. O'Brian, ''Analysis of Atmospheric Interferometer Data,'' AFGL-TR-84-0177, 1984.

24. R. Isaacs, S. Clough, R. Worsham, J. Moncet, B. Lindner, and L. Kaplan, ''Path Characterization Algorithms for FASCODE,'' Tech Report GL-TR-90-0080, AFGL, 1990; ADA#231914.

25. F. X. Kneizys, E. Shettle, W. O. Gallery, J. Chetwynd, L. Abreu, J. Selby, S. Clough, and R. Fenn, ''Atmospheric Transmittance/Radiance: Computer code LOWTRAN6,'' AFGL TR-83-0187, 1983; ADA#137786.

26. F. X. Kneizys, E. Shettle, L. Abreu, J. Chetwynd, G. Anderson, W. O. Gallery, J. E. A. Selby, and S. Clough, ''Users guide to LOWTRAN7,'' AFGL TR-88-0177, 1988; ADA#206773.

27. The HITRAN, LOWTRAN, and FASCODE programs can be ordered in a magnetic tape format from the U.S. Department of Commerce, National Climatic Data Center of NOAA, Federal Building, Asheville, NC 28801 (USA); HITRAN in a CD-ROM format is available from L. Rothman, Phillips Laboratory, GPOS, Hanscom AFB, MA 01731-3013, or from ONTAR Corp., 9 Village Way, North Andover, MA 01845-2000.

28. PClnTRAN and PCTRAN computer programs, ONTAR Corp., 9 Village Way, North Andover, MA 01845-2000.

29. HITRAN-PC database and TRANS Program, USF Research Foundation, University of South Florida, Tampa 33620 (USA).

30. LAB_CALC, Galactic Industries, 395 Main St., Salem, NH, 03079 USA; NIST/EPA Gas Phase Infrared Database, U.S. Dept. of Commerce, NIST, Standard Ref. Data, Gaithersburg, MD 20899; Infrared Analytics, 1424 N. Central Park Ave, Anaheim, CA 92802; Aldrich Library of Spectra, Aldrich Co., Milwaukee, WS 53201; Sadtler Spectra Data, Philadelphia, PA 19104-2596; Coblentz Society, P.O. Box 9952, Kirkwood, MO 63122.

31. R. S. Lawrence, G. R. Ochs, and S. F. Clifford, ''Measurements of Atmospheric Turbulence Relevant to Optical Propagation,'' *J. Opt. Soc. Am.* **60:**826–830 (1970).

32. M. A. Kallistratova and D. F. Timanovskiy, ''The Distribution of the Structure Constant of Refractive Index Fluctuations in the Atmospheric Surface Layer,'' *Iz. Atmos. Ocean. Phys.* **7:**46–48 (1971).

33. A. S. Monin and A. M. Obukhov, ''Basic Laws of Turbulent Mixing in the Ground Layer of the Atmosphere,'' *Trans. Geophys. Inst. Akad. Nauk. USSR* **151:**163–187 (1954).

34. A. S. Monin and A. M. Yaglom, *Statistical Fluid Mechanics: Mechanics of Turbulence,* MIT Press, Cambridge, 1971.

35. J. C. Wyngaard, Y. Izumi, and S. A. Collins, Jr., ''Behavior of the Refractive-index-structure Parameter Near the Ground,'' *J. Opt. Soc. Am.* **61:**1646–1650 (1971).

36. L. R. Tsvang, ''Microstructure of Temperature Fields in the Free Atmosphere,'' *Radio Sci.* **4:**1175–1177 (1969).

37. A. S. Frisch and G. R. Ochs, ''A Note on the Behavior of the Temperature Structure Parameter in a Convective Layer Capped by a Marine Inversion,'' *J. Appl. Meteorol.* **14:**415–419 (1975).

38. K. L. Davidson, T. M. Houlihan, C. W. Fairall, and G. E. Schader, ''Observation of the Temperature Structure Function Parameter, C_T^2, over the Ocean,'' *Boundary-Layer Meteorol.* **15:**507–523 (1978).

39. K. E. Kunkel, D. L. Walters, and G. A. Ely, "Behavior of the Temperature Structure Parameter in a Desert Basin," *J. Appl. Meteorol.* **15:**130–136 (1981).

40. W. Kohsiek, "Measuring C_T^2, C_Q^2, and C_{T_Q} in the Unstable Surface Layer, and Relations to the Vertical Fluxes of Heat and Moisture," *Boundary-Layer Meteorol,* **24:**89–107 (1982).

41. M. S. Belen'kiy, V. V. Boronyev, N. Ts. Gomboyev, and V. L. Mironov, *Sounding of Atmospheric Turbulence,* Nauka, Novosibirsk, 1986, p. 114.

42. A. A. M. Holtslag and A. P. Van Ulden, "A Simple Scheme for Daytime Estimates of the Surface Fluxes from Routine Weather Data," *J. Clim. Appl. Meteorol.* **22:**517–529 (1983).

43. T. Thiermann and A. Kohnle, "A Simple Model for the Structure Constant of Temperature Fluctuations in the Lower Atmosphere," *J. Phys. D: Appl. Phys.* **21:**S37–S40 (1988).

44. E. A. Andreas, "Estimating C_n^2 over Snow and Sea Ice from Meteorological Data," *J. Opt. Soc. Am. A* **5:**481–494 (1988).

45. J. L. Bufton, P. O. Minott, and M. W. Fitzmaurice, "Measurements of Turbulence Profiles in the Troposphere," *J. Opt. Soc. Am.* **62:**1068–1070 (1972).

46. F. W. Eaton, W. A. Peterson, J. R. Hines, K. R. Peterman, R. E. Good, R. R. Beland, and J. W. Brown, "Comparisons of VHF Radar, Optical, and Temperature Fluctuation Measurements of C_n^2, r_0, and Θ_0," *Theor. Appl. Climatol.* **39:**17–29 (1988).

47. F. Dalaudier, M. Crochet, and C. Sidi, "Direct Comparison between in situ and Radar Measurements of Temperature Fluctuation Spectra: A Puzzling Result," *Radio Sci.* **24:**311–324 (1989).

48. D. W. Beran, W. H. Hooke, and S. F. Clifford, "Acoustic Echo-sounding Techniques and Their Application to Gravity-wave, Turbulence, and Stability Studies," *Boundary-Layer Meteorol.* **4:**133–153 (1973).

49. M. Fukushima, K. Akita, and H. Tanaka, "Night-time Profiles of Temperature Fluctuations Deduced from Two-year Solar Observation," *J. Meteorol. Soc. Jpn.* **53:**487–491 (1975).

50. D. N. Asimakopoulis, R. S. Cole, S. J. Caughey, and B. A. Crease, "A Quantitative Comparison between Acoustic Sounder Returns and the Direct Measurement of Atmospheric Temperature Fluctuations," *Boundary-Layer Meteorol.* **10:**137–147 (1976).

51. T. E. VanZandt, J. L. Green, K. S. Gage, and W. L. Clark, "Vertical Profiles of Refractivity Turbulence Structure Constant: Comparison of Observations by the Sunset Radar with a New Theoretical Model," *Radio Sci.* **13:**819–829 (1978).

52. K. S. Gage and B. B. Balsley, "Doppler Radar Probing of the Clear Atmosphere," *Bull. Am. Meteorol. Soc.* **59:**1074–1093 (1978).

53. R. B. Chadwick and K. P. Moran, "Long-term measurements of C_n^2 in the Boundary Layer," *Raio Sci.* **15:**355–361 (1980).

54. B. B. Balsley and V. L. Peterson, "Doppler-radar Measurements of Clear Air Turbulence at 1290 MHz," *J. Appl. Meteorol.* **20:**266–274 (1981).

55. E. E. Gossard, R. B. Chadwick, T. R. Detman, and J. Gaynor, "Capability of Surface-based Clear-air Doppler Radar for Monitoring Meteorological Structure of Elevated Layers," *J. Clim. Appl. Meteorol.* **23:**474 (1984).

56. G. D. Nastrom, W. L. Ecklund, K. S. Gage, and R. G. Strauch, "The Diurnal Variation of Backscattered Power from VHF Doppler Radar Measurements in Colorado and Alaska," *Radio Sci.* **20:**1509–1517 (1985).

57. D. L. Fried, "Remote Probing of the Optical Strength of Atmospheric Turbulence and of Wind Velocity," *Proc. IEEE* **57:**415–420 (1969).

58. J. W. Strohbehn, "Remote Sensing of Clear-air Turbulence," *J. Opt. Soc. Am.* **60:**948 (1970).

59. J. Vernin and F. Roddier, "Experimental Determination of Two-dimensional Power Spectra of Stellar Light Scintillation. Evidence for a Multilayer Structure of the Air Turbulence in the Upper Troposphere," *J. Opt. Soc. Am.* **63:**270–273 (1973).

60. G. R. Ochs, T. Wang, R. S. Lawrence, and S. F. Clifford, "Refractive Turbulence Profiles Measured by One-dimensional Spatial Filtering of Scintillations," *Appl. Opt.* **15:**2504–2510 (1976).

61. R. E. Hufnagel and N. R. Stanley, "Modulation Transfer Function Associated with Image Transmission through Turbulent Media," *J. Opt. Soc. Am.* **54:**52–61 (1964).

62. R. E. Hufnagel, "Variations of Atmospheric Turbulence," in *Technical Digest of Topical Meeting on Optical Propagation through Turbulence,* Optical Society of America, Washington, D.C., 1974.

63. R. J. Sasiela, *A Unified Approach to Electromagnetic Wave Propagation in Turbulence and the Evaluation of Multiparameter Integrals,* Technical Report 807, MIT Lincoln Laboratory, Lexington, 1988.

64. V. A. Banakh and V. L. Mironov, *Lidar in a Turbulent Atmosphere,* Artech House, Boston, 1987.

65. C. W. Fairall and R. Markson, "Aircraft Measurements of Temperature and Velocity Microturbulence in the Stably Stratified Free Troposphere," *Proceedings of the Seventh Symposium on Turbulence and Diffusion,* November 12–15, 1985, Boulder, Co.

66. J. C. Kaimal, *The Atmospheric Boundary Layer—Its Structure and Measurement,* Indian Institute of Tropical Meteorology, Pune, 1988.

67. J. Weinstock, "Vertical Turbulent Diffusion in a Stably Stratified Fluid," *J. Atmos. Sci.* **35:**1022–1027 (1978).

68. J. Barat and F. Bertin, "On the Contamination of Stratospheric Turbulence Measurements by Wind Shear," *J. Atmos. Sci.* **41:**819–827 (1984).

69. C. E. Coulman, J. Vernin, Y. Coqueugniot, and J. L. Caccia, "Outer Scale of Turbulence Appropriate to Modeling Refractive-index Structure Profiles," *Appl. Opt.* **27:**155–160 (1988).

70. C. E. Coulman and J. Vernin, "Significance of Anisotropy and the Outer Scale of Turbulence for Optical and Radio Seeing," *Appl. Opt.* **30:**118–126 (1991).

71. M. M. Colavita, "Design Considerations for Very Long Baseline Fringe-tracking Interferometers," *Proc. SPIE* **1237:**80–86 (1990).

72. L. A. Chernov, *Wave Propagation in a Random Medium,* Dover, New York, 1967, p. 26.

73. P. Beckmann, "Signal Degeneration in Laser Beams Propagated through a Turbulent Atmosphere," *Radio Sci.* **69D:**629–640 (1965).

74. T. Chiba, "Spot Dancing of the Laser Beam Propagated through the Atmosphere," *Appl. Opt.* **10:**2456–2461 (1971).

75. J. H. Churnside and R. J. Lataitis, "Wander of an Optical Beam in the Turbulent Atmosphere," *Appl. Opt.* **29:**926–930 (1990).

76. G. A. Andreev and E. I. Gelfer, "Angular Random Walks of the Center of Gravity of the Cross Section of a Diverging Light Beam," *Radiophys. Quantum Electron.* **14:**1145–1147 (1971).

77. M. A. Kallistratova and V. V. Pokasov, "Defocusing and Fluctuations of the Displacement of a Focused Laser Beam in the Atmosphere," *Radiophys. Quantum Electron.* **14:**940–945 (1971).

78. J. A. Dowling and P. M. Livingston, "Behavior of Focused Beams in Atmospheric Turbulence: Measurements and Comments on the Theory," *J. Opt. Soc. Am.* **63:**846–858 (1973).

79. J. R. Dunphy and J. R. Kerr, "Turbulence Effects on Target Illumination by Laser Sources: Phenomenological Analysis and Experimental Results," *Appl. Opt.* **16:**1345–1358 (1977).

80. V. I. Klyatskin and A. I. Kon, "On the Displacement of Spatially Bounded Light Beams in a Turbulent Medium in the Markovian-random-process Approximation," *Radiophys. Quantum Electron.* **15:**1056–1061 (1972).

81. A. I. Kon, V. L. Mironov, and V. V. Nosov, "Dispersion of Light Beam Displacements in the Atmosphere with Strong Intensity Fluctuations," *Radiophys. Quantum Electron.* **19:**722–725 (1976).

82. V. L. Mironov and V. V. Nosov, "On the Theory of Spatially Limited Light Beam Displacements in a Randomly Inhomogeneous Medium," *J. Opt. Soc. Am.* **67:**1073–1080 (1977).

83. R. F. Lutomirski and H. T. Yura, "Propagation of a Finite Optical Beam in an Inhomogeneous Medium" *Appl. Opt.* **10:**1652–1658 (1971).

84. R. F. Lutomirski and H. T. Yura, "Wave Structure Function and Mutual Coherence Function of an Optical Wave in a Turbulent Atmosphere," *J. Opt. Soc. Am.* **61:**482–487 (1971).

85. H. T. Yura, "Atmospheric Turbulence Induced Laser Beam Spread," *Appl. Opt.* **10:**2771–2773 (1971).

86. H. T. Yura, "Mutual Coherence Function of a Finite Cross Section Optical Beam Propagating in a Turbulent Medium," *Appl. Opt.* **11:**1399–1406 (1972).

87. H. T. Yura, "Optical Beam Spread in a Turbulent Medium: Effect of the Outer Scale of Turbulence," *J. Opt. Soc. Am.* **63:**107–109 (1973).

88. H. T. Yura, "Short-term Average Optical-beam Spread in a Turbulent Medium," *J. Opt. Soc. Am.* **63:**567–572 (1973).

89. M. T. Tavis and H. T. Yura, "Short-term Average Irradiance Profile of an Optical Beam in a Turbulent Medium," *Appl. Opt.* **15:**2922–2931 (1976).

90. R. L. Fante, "Electromagnetic Beam Propagation in Turbulent Media," *Proc. IEEE* **63:**1669–1692 (1975).

91. R. L. Fante, "Electromagnetic Beam Propagation in Turbulent Media: An Update," *Proc. IEEE* **68:**1424–1443 (1980).

92. G. C. Valley, "Isoplanatic Degradation of Tilt Correction and Short-term Imaging Systems," *Appl. Opt.* **19:**574–577 (1980).

93. H. J. Breaux, *Correlation of Extended Huygens-Fresnel Turbulence Calculations for a General Class of Tilt Corrected and Uncorrected Laser Apertures,* Interim Memorandum Report No. 600, U.S. Army Ballistic Research Laboratory, 1978.

94. D. M. Cordray, S. K. Searles, S. T. Hanley, J. A. Dowling, and C. O. Gott, "Experimental Measurements of Turbulence Induced Beam Spread and Wander at 1.06, 3.8, and 10.6 μm," *Proc. SPIE* **305:**273–280 (1981).

95. S. K. Searles, G. A. Hart, J. A. Dowling, and S. T. Hanley, "Laser Beam Propagation in Turbulent Conditions," *Appl. Opt.* **30:**401–406 (1991).

96. J. H. Churnside and R. J. Lataitis, "Angle-of-arrival Fluctuations of a Reflected Beam in Atmospheric Turbulence," *J. Opt. Soc. Am. A* **4:**1264–1272 (1987).

97. D. L. Fried, "Optical Resolution through a Randomly Inhomogeneous Medium for Very Long and Very Short Exposures," *J. Opt. Soc. Am.* **56:**1372–1379 (1966).

98. R. F. Lutomirski, W. L. Woodie, and R. G. Buser, "Turbulence-degraded Beam Quality: Improvement Obtained with a Tilt-correcting Aperture," *Appl. Opt.* **16:**665–673 (1977).

99. D. L. Fried, "Statistics of a Geometrical Representation of Wavefront Distortion," *J. Opt. Soc. Am.* **55:**1427–1435 (1965); **56:**410 (1966).

100. D. M. Chase, "Power Loss in Propagation through a Turbulent Medium for an Optical-heterodyne System with Angle Tracking," *J. Opt. Soc. Am.* **56:**33–44 (1966).

101. J. H. Churnside and C. M. McIntyre, "Partial Tracking Optical Heterodyne Receiver Arrays," *J. Opt. Soc. Am.* **68:**1672–1675 (1978).

102. V. I. Tatarskii, *The Effects of the Turbulent Atmosphere on Wave Propagation,* Israel Program for Scientific Translations, Jerusalem, 1971.

103. R. W. Lee and J. C. Harp, "Weak Scattering in Random Media, with Applications to Remote Probing," *Proc. IEEE* **57:**375–406 (1969).

104. R. S. Lawrence and J. W. Strohbehn, "A Survey of Clear-air Propagation Effects Relevant to Optical Communications," *Proc. IEEE* **58:**1523–1545 (1970).

105. S. F. Clifford, "The Classical Theory of Wave Propagation in a Turbulent Medium," in J. W. Strohbehn (ed.), *Laser Beam Propagation in the Atmosphere,* Springer-Verlag, New York, 1978, pp. 9–43.

106. A. I. Kon and V. I. Tatarskii, "Parameter Fluctuations of a Space-limited Light Beam in a Turbulent Atmosphere," *Izv. VUZ Radiofiz.* **8:**870–875 (1965).

107. R. A. Schmeltzer, "Means, Variances, and Covariances for Laser Beam Propagation through a Random Medium," *Quart. J. Appl. Math.* **24:**339–354 (1967).

108. D. L. Fried and J. B. Seidman, "Laser-beam Scintillation in the Atmosphere," *J. Opt. Soc. Am.* **57:**181–185 (1967).

109. D. L. Fried, "Scintillation of a Ground-to-Space Laser Illuminator," *J. Opt. Soc. Am.* **57:**980–983 (1967).

110. Y. Kinoshita, T. Asakura, and M. Suzuki, "Fluctuation Distribution of a Gaussian Beam Propagating through a Random Medium," *J. Opt. Soc. Am.* **58:**798–807 (1968).

111. A. Ishimaru, "Fluctuations of a Beam Wave Propagating through a Locally Homogeneous Medium," *Radio Sci.* **4:**295–305 (1969).

112. A. Ishimaru, "Fluctuations of a Focused Beam Wave for Atmospheric Turbulence Probing," *Proc. IEEE* **57:**407–414 (1969).

113. A. Ishimaru, "The Beam Wave Case and Remote Sensing," in J. W. Strohbehn (ed.), *Laser Beam Propagation in the Atmosphere,* Springer-Verlag, New York, 1978, pp. 129–170.

114. P. J. Titterton, "Scintillation and Transmitter-aperture Averaging over Vertical Paths," *J. Opt. Soc. Am.* **63:**439–444 (1973).

115. H. T. Yura and W. G. McKinley, "Optical Scintillation Statistics for IR Ground-to-Space Laser Communication Systems," *Appl. Opt.* **22:**3353–3358 (1983).

116. P. A. Lightsey, J. Anspach, and P. Sydney, "Observations of Uplink and Retroreflected Scintillation in the Relay Mirror Experiment," *Proc. SPIE* **1482** (in press) (1991).

117. D. L. Fried, "Aperture Averaging of Scintillation," *J. Opt. Soc. Am.* **57:**169–175 (1967).

118. J. H. Churnside, "Aperture Averaging of Optical Scintillations in the Turbulent Atmosphere," *Appl. Opt.* **30:**1982–1994 (1991).

119. J. H. Churnside and R. G. Frehlich, "Experimental Evaluation of Log-normally Modulated Rician and IK Models of Optical Scintillation in the Atmosphere," *J. Opt. Soc. Am. A* **6:**1760–1766 (1989).

120. G. Parry and P. N. Pusey, "K Distributions in Atmospheric Propagation of Laser Light," *J. Opt. Soc. Am.* **69:**796–798 (1979).

121. G. Parry, "Measurement of Atmospheric Turbulence Induced Intensity Fluctuations in a Laser Beam," *Opt. Acta* **28:**715–728 (1981).

122. W. A. Coles and R. G. Frehlich, "Simultaneous Measurements of Angular Scattering and Intensity Scintillation in the Atmosphere," *J. Opt. Soc. Am.* **72:**1042–1048 (1982).

123. J. H. Churnside and S. F. Clifford, "Lognormal Rician Probability-density Function of Optical Scintillations in the Turbulent Atmosphere," *J. Opt. Soc. Am. A* **4:**1923–1930 (1987).

124. R. Dashen, "Path Integrals for Waves in Random Media," *J. Math. Phys.* **20:**894–920 (1979).

125. K. S. Gochelashvily and V. I. Shishov, "Multiple Scattering of Light in a Turbulent Medium," *Opt. Acta* **18:**767–777 (1971).

126. K. S. Gochelashvily, V. G. Pevgov, and V. I. Shishov, "Saturation of Fluctuations of the Intensity of Laser Radiation at Large Distances in a Turbulent Atmosphere (Fraunhofer Zone of Transmitter)," *Sov. J. Quantum Electron.* **4:**632–637 (1974).

127. A. M. Prokhorov, F. V. Bunkin, K. S. Gochelashvily, and V. I. Shishov, "Laser Irradiance Propagation in Turbulent Media," *Proc. IEEE* **63:**790–810 (1975).

128. R. L. Fante, "Inner-scale Size Effect on the Scintillations of Light in the Turbulent Atmosphere," *J. Opt. Soc. Am.* **73:**277–281 (1983).

129. R. G. Frehlich, "Intensity Covariance of a Point Source in a Random Medium with a Kolmogorov Spectrum and an Inner Scale of Turbulence," *J. Opt. Soc. Am. A.* **4:**360–366 (1987).

130. J. H. Churnside and R. J. Hill, "Probability Density of Irradiance Scintillations for Strong Path-integrated Refractive Turbulence," *J. Opt. Soc. Am. A.* **4:**727–733 (1987).

131. D. K. Killinger and A. Mooradian (eds.), *Optical and Laser Remote Sensing,* Springer-Verlag, Optical Sciences, vol. 39, 1983.

132. L. J. Radziemski, R. W. Solarz, and J. A. Paisner (eds.), *Laser Spectroscopy and Its Applications,* Marcel Dekker, Optical Eng., vol. 11, 1987.

133. T. Kobayashi, "Techniques for Laser Remote Sensing of the Environment," *Remote Sensing Reviews,* **3:**1–56 (1987).

134. E. D. Hinkley (ed.), *Laser Monitoring of the Atmosphere,* Springer-Verlag, Berlin, 1976.

135. W. B. Grant and R. T. Menzies, "A Survey of Laser and Selected Optical Systems for Remote Measurement of Pollutant Gas Concentrations," *APCA Journal* **33:**187 (1983).

136. "Optical Remote Sensing of the Atmosphere," *Conf. Proceedings, OSA Topical Meeting,* Williamsburg, 1991.

137. P. B. Hays, V. J. Abreu, D. A. Gell, H. J. Grassl, W. R. Skinner, and M. E. Dobbs, "The High Resolution Doppler Imager on the Upper Atmospheric Research Satellite," *J. Geophys. Res. (Atmosphere)* **98:**10713 (1993); P. B. Hays, V. J. Abreu, M. D. Burrage, D. A. Gell, A. R. Marshall, Y. T. Morton, D. A. Ortland, W. R. Skinner, D. L. Wu, and J. H. Yee, "Remote Sensing of Mesospheric Winds with the High Resolution Imager," *Planet. Space Sci.* **40:**1599 (1992).

138. E. Browell, "Differential Absorption Lidar Sensing of Ozone," *Proc. IEEE* **77:**419 (1989).

139. J. M. Intrieri, A. J. Dedard, and R. M. Hardesty, "Details of Colliding Thunderstorm Outflow as Observed by Doppler Lidar," *J. Atmospheric Sciences* **47:**1081 (1990); R. M. Hardesty, K. Elmore, M. E. Jackson, in *21st Conf. on Radar Meteorology,* American Meteorology Society, Boston, 1983.

140. M. P. McCormick and R. E. Veiga, "Initial Assessment of the Stratospheric and Climatic Impact of the 1991 Mount Pinatubo Eruption—Prolog," *Geophysical Research Lett.* **19:**155 (1992).

141. R. A. R. Tricker, *Introduction to Meteorological Optics,* American Elsevier, New York, 1970.

142. R. Greenler, *Rainbows, Halos, and Glories,* Cambridge University Press, 1980.